The Inland Maintenance and Re-intensification of Tropical Storm Bill (2015) Part 2: Precipitation Microphysics

Noah S. Brauer*

University of Oklahoma, School of Meteorology, Advanced Radar Research Center, Norman, Oklahoma

Jeffrey B. Basara

University of Oklahoma, School of Meteorology, School of Civil Engineering and Environmental Science, Norman, Oklahoma, USA

Pierre E. Kirstetter

University of Oklahoma, School of Meteorology, Advanced Radar Research Center, NOAA National Severe Storms Laboratory, Norman, Oklahoma

Ryann A. Wakefield

University of Oklahoma, School of Meteorology, Norman, Oklahoma, USA

Cameron R. Homeyer

University of Oklahoma, School of Meteorology, Norman, Oklahoma

Jinwoong Yoo

University of Maryland (ESSIC), NASA Goddard Space Flight Center

Marshall Shepherd

University of Georgia, Department of Geography

Joseph. A. Santanello, Jr.

NASA Goddard Space Flight Center

Corresponding author address: Noah S. Brauer, National Weather Center, 120 David L. Boren Blvd, Norman, OK 73072.

E-mail: nbrauer@ou.edu

ABSTRACT

Tropical Storm Bill produced over 400 mm of rainfall to portions of southern Oklahoma from 16-20 June 2015, adding to the catastrophic urban and river flooding that occurred throughout the region in the month prior to landfall. The unprecedented excessive precipitation event that occurred across Oklahoma and Texas during May and June 2015 resulted in anomalously high soil moisture and latent heat fluxes over the region, acting to increase the available boundary layer moisture. Tropical Storm Bill progressed inland over the region of anomalous soil moisture and latent heat fluxes which helped maintain polarimetric radar signatures associated with tropical, warm rain events. Vertical profiles of polarimetric radar variables such as Z_H, Z_{DR}, K_{DP}, and ρ_{hv} were analyzed in time and space over Texas and Oklahoma. The profiles suggest that Tropical Storm Bill maintained warm rain signatures and collision-coalescence processes as it tracked hundreds of kilometers inland away from the landfall point consistent with tropical cyclone precipitation characteristics. Dual-frequency precipitation radar observations from the NASA GPM DPR were also analyzed post-landfall and showed similar signatures of collision-coalescence while Bill moved over north Texas, southern Oklahoma, eastern Missouri, and western Kentucky.

1. Introduction

Landfalling tropical cyclones (TCs) can produce significant destruction and mortality, and have been estimated to kill upwards of 500 million people since 1492 (Rappaport 2000). While damaging winds pose a threat to life and property near the TC landfall point, freshwater flooding can result in human fatalities hundreds of kilometers inland (e.g., Rappaport 2000; Jarrell et al. 2001). Thus, it is important to understand the characteristics of excessive precipitation in landfalling TCs well away from coastal regions.

May and June 2015 produced unprecedented rainfall in portions of Oklahoma and Texas, including an all-time high rainfall total of 594 mm for the month of May at the Norman Mesonet site (e.g., Brock et al. 1995; McPherson et al. 2007; Duchon et al. 2017). As a result, catastrophic urban and river flooding occurred during this period due to excessive precipitation, runoff, and saturated soils, resulting in 11 fatalities. Tropical Storm Bill further contributed to the excessive precipitation event over the region as it tracked over Texas and Southern Oklahoma in June 2015.

Previous studies (e.g., Clark and Arritt 1995; Lynn et al. 1998) have shown the importance of soil moisture on generating deep convection through enhanced latent heat fluxes which serves to increase boundary layer moisture. The influence of soil moisture on local weather and climate extremes is most pronounced in continental regions characterized by a transition zone from humid to drier climates (e.g., Guo et al. 2006; Koster et al. 2006), such as the Southern Great Plains (SGP). In this region, evapotranspiration displays a greater sensitivity to changes in both soil moisture and atmospheric demand (e.g., Guo et al. 2006; Koster et al. 2011; Wei et al. 2015). The connection between these continental land-atmosphere feedbacks and TCs is not entirely obvious at first. However, observations of TC re-intensification over land have recently given rise to the concept of the ”Brown Ocean Effect”, which hypothesizes that anomalously moist soils can mimic an oceanic surface by providing fluxes of heat and moisture to the TC (e.g., Emanuel et al. 2008; Andersen and Shepherd 2014a).

The first paper of this study (Wakefield et al. 2020) found that the brown ocean effect played a role in maintaining Tropical Storm Bill over land through above average latent heat fluxes which increases total precipitable water and vertically integrated relative humidity. The re-intensification of Tropical Storm Erin (2007) over Oklahoma has been attributed to this particular phenomenon (e.g., Arndt et al. 2009; Monteverdi and Edwards 2010; Evans et al. 2011; Kellner et al. 2011; Andersen and Shepherd 2014a). Nair et al. (2019) recently attributed the historic flooding in Louisiana associated with an unnamed tropical system to the ”Brown Ocean Effect”. TC maintenance and/or re-intensification events, otherwise known as TCMI events, have been observed globally (Andersen and Shepherd 2014a), and are typically associated with above normal latent heat flux in the 3-weeks prior to the TC’s landfall.

Andersen and Shepherd (2014b) used a 900-600 mb thermal wind calculation to categorize landfalling TCs after progressing inland as having a warm core, neutral (hybrid), or cold core. From the 227 cases examined, 45 TCs were found to have re-intensified over land, primarily due to large positive heat fluxes over a warm and moist land surface. Other important factors that were found to be conducive to TCMI over land are weak deep-layer wind shear and a lack of a horizontal temperature gradient. While synoptic-scale features and land surface characteristics were found to dictate TCMIs over land (e.g., Andersen and Shepherd 2014a; Yoo et al. 2020), the microphysical precipitation processes remain to be explored in these events. Specifically, the evolution and quantification of microphysical processes have yet to be systematically analyzed in cases of inland TC re-intensification or maintenance. Griffin et al. (2014) performed an in-depth ground-based polarimetric radar analysis of Tropical Storm Erin’s re-intensification over central Oklahoma. Didlake and Kumjian (2017) examined the interaction between storm asymmetries, vertical wind shear, and precipitation processes using polarimetric radar observations in Hurricane Arthur (2014), and found that vertical profiles of Z_H and Z_{DR} in the downshear half of the eyewall exhibited signatures associated with collision-coalescence. Feng and Bell (2019) performed a similar analysis in Hurricane Harvey (2017) and discussed size-sorting signatures in the eyewall as the maximum in K_{DP} and Z_H remained downwind from the maximum in Z_{DR}. Polarimetric radar observations from the WSR-88D network (Crum and Alberty 1993) provide additional insight into the evolution of precipitation processes, and for example can be used to diagnose the extent of the low-echo centroid, warm rain processes (i.e., collision-coalescence and drop breakup) that are expected in a TC environment (e.g., Ryzhkov et al. 2005b; Vitale and Ryan 2013; Kumjian and Prat 2014; Didlake and Kumjian 2017).

Polarimetric radar observations at essentially unattenuated frequencies provide physical insight into precipitation processes at a high temporal resolution (e.g., Medlin et al. 2007; Didlake Jr. and Kumjian 2018), and can provide valuable insight into precipitation microphysics and drop size distribution characteristics that can ultimately improve the accuracy of quantitative precipitation estimation (e.g., Seliga and Bringi 1976; Herzegh and Jameson 1992; Zrnić and Ryzhkov 1996; Ryzhkov et al. 2005a; Giangrande and Ryzhkov 2008; Cifelli et al. 2011). However, ground-radars are often limited in sampling the vertical dimension that is critical for precipitation microphysics, due to discrete elevation angles and increasing beam elevation with range, combined with beam broadening and non-uniform beam filling (Kirstetter et al. 2013). Other limitations include calibration uncertainty (e.g., Gorgucci et al. 1992; Bechini et al. 2008), the presence of mixed-phase precipitation (e.g., Gray et al. 2006; Kumjian 2013a), and partial beam filling (e.g., Ryzhkov 2007; Zhang et al. 2013). On the other hand, satellite-based radars provide a more regular and a finer vertical sampling as well as calibration stability, but they operate at attenuated frequencies. Thus, it is useful to jointly examine ground-based radar observations and satellite-borne radar retrievals to quantify microphysical processes (e.g., Smalley et al. 2017; Porcacchia et al. 2019). The synergy between ground-based radar observations and space-borne radar retrievals provide a novel framework for identifying instances of TCMI in Tropical Storm Bill by identifying profiles of collision-coalescence processes hundreds of kilometers inland from the landfall point. The objective of this study is to identify whether warm rain processes that are commonly observed in TCs existed well away from the landfall point during the periods of TCMI.

2. Data and Methods

a. Event Background

Tropical Storm Bill made landfall at 1645 UTC 16 June 2015 near Matagorda Island, TX with an estimated maximum sustained wind speed of 26 ms^{-1} (50 knots) and a minimum central pressure of 997 mb. Bill then progressed north over north Texas and into southeastern Oklahoma while maintaining tropical depression status before being classified as an extratropical cyclone as it moved east into Arkansas, Missouri, and Kentucky (Fig.1). Bill produced three distinct maxima in rainfall, with accumulations near the landfall point over south Texas near 300 mm, and a secondary maximum over north Texas and southern Oklahoma of 400 mm, and a third maximum over southern Illinois of 225 mm (Fig.2). From hereon, TCMI1 will refer to the period of tropical cyclone maintenance over north Texas and southern Oklahoma from 1200-1800 UTC 17 June, and TCMI2 will refer to the re-intensification of Bill over southern Missouri, Illinois, and western Kentucky from 1200 UTC 19 June to 1200 UTC 20 June (Wakefield et al. 2020).

b. Polarimetric Radar Data

Tropical Storm Bill offers the first opportunity to examine TCMI over land and the entire microphysical evolution of the cyclone using polarimetric radar observations since the WSR-88D network was upgraded with dual-polarization technology in 2010. Thus, Tropical Storm Erin (2007) was not captured due to a limited radar network that contained dual-polarization capabilities. This study uses Level-II WSR-88D data from the National Centers for Environmental Information (NOAA National Weather Service (NWS) Radar Operations Center 1991), which are then processed using the Gridded NEXRAD WSR-88D (GridRad) software (Bowman and Homeyer 2017). These data have a temporal resolution of 5 minutes and have an azimuthal resolution of 0.5^o for the lowest four elevation angles, and a 1^o azimuthal resolution for other angles (Crum and Alberty 1993).

The polarimetric radar variables that are analyzed include the horizontal reflectivity factor (Z_H), differential reflectivity (Z_{DR}), specific differential phase (K_{DP}), and the co-polar correlation coefficient (ρ_{hv}). Z_H is proportional to the integration of the diameter of scatterers raised to the sixth power and provides information regarding the size and concentration of precipitation-sized hydrometeors that satisfy the Rayleigh regime (e.g., Austin 1987; Herzegh and Jameson 1992; Zrnic and Ryzhkov 1999; Vitale and Ryan 2013). Z_{DR} is defined as the difference between the horizontal and vertical reflectivity factors, and provides information about the size, shape, and orientation of hydrometeors (e.g., Seliga and Bringi 1976; Herzegh and Jameson 1992). Z_{DR} observations can be biased if mixed-phase precipitation is present within a resolution volume which can lead to non-uniform beam filling (e.g., Bringi et al. 1990; Testud et al. 2000; Ryzhkov 2007; Giangrande and Ryzhkov 2008), or if the radar is miscalibrated (e.g., Gorgucci et al. 1992; Bechini et al. 2008). K_{DP} is influenced by the number concentration of hydrometeors within a volume (e.g., Kumjian 2013b). This is because large drops are oblate spheroids, therefore the horizontal polarization will encounter more of a phase shift compared to the vertical polarization, resulting in positive K_{DP} (e.g., Herzegh and Jameson 1992; Zrnic and Ryzhkov 1999; Ryzhkov et al. 2005b; Kumjian 2013a). Thus, one advantage of using K_{DP} is that it is independent of radar calibration and is immune to propagation attenuation, which makes it useful for estimating heavy rainfall (e.g., Seliga and Bringi 1978; Jameson 1985; Wang and Chandrasekar 2009). ρ_{hv} is a measure of the similarity of scatters in a resolution volume (e.g., Herzegh and Jameson 1992; Zrnic and Ryzhkov 1999; Ryzhkov et al. 2005b; Ryzhkov et al. 2005a; Kumjian 2013a). A homogeneous particle size distribution will yield a ρ_{hv} close to 1, whereas mixed-phased precipitation will result in a ρ_{hv} <0.9 (e.g., Herzegh and Jameson 1992; Zrnic and Ryzhkov 1999; Ryzhkov et al. 2005b; Ryzhkov et al. 2005a; Kumjian 2013a).

Rainfall in TCs are characterized by a larger concentration of smaller drops (e.g., Cao et al. 2008; Brauer et al. 2020; DeHart and Bell 2020). Thus, Z_H tends to be lower than that of rainfall in the mid-latitudes due to the dependence of Z_H on drop size (e.g., Austin 1987; Herzegh and Jameson 1992; Zrnic and Ryzhkov 1999). Further, due to the large number concentration of small drops found in TCs (e.g., Squires 1956; Ulbrich and Atlas 2007; Xu et al. 2008), Z_{DR} tends to range from 0-1 dB and K_{DP} tends to be positive (e.g., Brown et al. 2016; Didlake and Kumjian 2017). In terms of vertical structure, the warm rain events associated with TCs that are characterized by the aforementioned polarimetric radar signatures are typically dominated by collision-coalescence (CC) below the -10^oC isotherm because supercooled liquid water can still contribute to drop growth via the CC mechanism (e.g., Vitale and Ryan 2013; Schroeder et al. 2016). Signatures of CC below the -10^oC isotherm are identified by Z_H and Z_{DR} increasing towards the surface (e.g., Xu et al. 2008; Kumjian and Prat 2014; Carr et al. 2017; Porcacchia et al. 2019).

Time-height curtains of the polarimetric radar variables were plotted on from 1200 UTC 16 June to 0000 UTC 17 June near the landfall point at El Campo, TX (29.20^oN, -96.27^oW) and from 1200 UTC 17 June to 0000 UTC 18 June approximately 600 km inland at Grady, OK (35.05^oN, -97.87^oW) using a 5-point spatial mean surrounding the point of interest, similar to the quasi-vertical profile methodology in Ryzhkov et al. (2016). Additionally, vertical profiles of drop size were plotted to identify regions of drop growth and CC below the $-10^{o}C$ isotherm. To estimate drop size, a Z_{DR} and K_{DP}-weighted relationship for tropical rainfall was used (Gorgucci et al. 2002) and is expressed in Equation 1. An identical framework was used to plot time-height curtains from 1800-0000 UTC 19-20 June over Cape Girardeau, MO ($37.30^{o}N$, $-89.53^{o}W$) and 1200-0000 UTC 19-20 June over Cairo, IL ($37.00^{o}N$, $-89.18^{o}W$) to gain insight into dominant microphysical processes during TCMI2.

$$\hat{D_o} = 1.155(K_{DP})^{0.076}(Z_{DR})^{1.164} \tag{1}$$

Contoured Frequency by Altitude Diagrams (CFADs) were plotted at each of the four locations using the ground-based radar observations of Z_H, Z_{DR}, K_{DP}, and ρ_{hv}. Histograms were calculated at each level of constant altitude and plotted on a reflectivity versus height grid, with only values of Z_H, Z_{DR}, and K_{DP} where $\rho_{hv} > 0.97$ were retained.

c. GPM Dual Frequency Precipitation Radar Data

The Global Precipitation Measurements (GPM) mission was launched in 2014 as a successor to the Tropical Rainfall Measurement Mission (TRMM) which ended in 2015 (e.g., Hou et al. 2014; Skofronick-Jackson et al. 2017). Onboard the GPM core observatory is the active dual-frequency precipitation radar (DPR). The GPM DPR is generally well-calibrated, has a higher sensitivity than S-band radars such as the WSR-88D network, and can provide snapshots of vertical profiles of reflectivity at a high vertical resolution and a low temporal resolution (e.g., Kozu et al. 2001; Hou et al. 2014). The GPM DPR is also capable of estimating precipitation at the surface when rainfall rates exceed 0.5 mm $hour^{-1}$ (e.g., Kozu et al. 2001; Hou et al. 2014). Although the GPM DPR is specifically prone to attenuation, it allows for a complementary source of identification and quantification of precipitation processes in addition to the ground-based radar network.

Alternatively, the GPM DPR operates at both Ku and Ka bands (13.6 GHz), which allows for the detection of lighter rainfall and ice hydrometeors due to the higher sensitivity of the Ka-band (12 dBZ). This is particularly useful for precipitation estimation at higher latitudes where frozen precipitation and stratiform systems are more common (e.g., Skofronick-Jackson et al. 2017; Porcacchia et al. 2019). The GPM DPR has a horizontal resolution of 5 km and a vertical resolution of 250 m. In 2015, the swath widths were 245 km at Ku-band and 120 km at Ka-band (e.g., Hou et al. 2014; Skofronick-Jackson et al. 2017).

The GPM DPR alogirthm interprets the radar signal and estimates drop size distribution moments such as the mass-weighted mean drop diameter (D_M) and the generalizaed intercept parameter ($log_{10}(N_W)$), which is directly related to the number concentration of drops (GPM DPR Algorithm Theoretical Basis Document (ATBD)). These quantities are estimated assuming a gamma distribution function shown in equation (2), and computes D_M using the equation (3), where N_m is the corresponding scale factor and μ is the shape factor (Iguchi et al. 2018). The precipitation category algorithm identifies the presence of a bright-band, which is a signature in stratiform precipitation, and is used to partition areas into stratiform, convective, and other precipitation categories. More information regarding the algorithms used to calculate D_M and $log_{10}(N_W)$, and precipitation category can be found: (`https://gpm.nasa.gov/sites/default/files/document_files/ATBD_DPR_201811_with_Appendix3b_0.pdf`). Further, the 0^oC isotherm was also extracted from the GPM DPR and was plotted on the along-track cross-sections to quantify the melting layer height.

$$N(D) = N_m D^{\mu} exp\left[-\frac{(4+\mu)D}{D_M}\right] \tag{2}$$

$$D_M = \frac{\int D^4 N(D) dD}{\int D^3 N(D) dD} \quad (3)$$

Two GPM overpasses occurred over Texas and Oklahoma on 17 June at 0538 UTC and 1454 UTC as Tropical Storm Bill progressed inland over the region. Along-track vertical profiles of attenuation-corrected reflectivity at Ku-band were extracted through the inner core of Bill to identify regions of CC below the melting level. Regions of CC were identified in regions where reflectivity increases towards the surface below the melting level, which indicates drop growth and a resulting increase in reflectivity (Porcacchia et al. 2019). This reflectivity enhancement can also be caused by other factors such as the the height of the melting layer and the environmental lapse rate (Grams et al. 2014). Vertical profiles of D_M and $log_{10}(N_W)$ were also examined along the same ray to quantify drop size and drop number concentration variation with height. An additional GPM overpass occurred over southern Illinois at 0436 UTC on 20 June which provided an additional opportunity to quantify the extent of warm rain processes and TCMI as Bill progressed inland.

d. Miscellaneous Data

The Hurricane Database (HURDAT2) best-track data was used to plot the track of Tropical Storm Bill from 16-21 June, 2015 (Science Applications International Corporation and National Hurricane Center 1993). The ECMWF ERA-5 dataset has a horizontal grid spacing 31 km, 137 vertical levels, and a 3 hour temporal resolution (Hersbach et al. 2019), and was used to generate longitude-height cross-sections of potential vorticity, potential temperature, and vertical velocity during both periods of the TCMIs (i.e., TCMI1 and TCMI2). The Parameter-elevation Regressions on Independent Model (PRISM; Daly et al. 1994) which uses a 4 km grid resolution was used for daily precipitation accumulation from 16-20 June over Oklahoma and Texas. Additionally, the University of Wyoming sounding database was used to plot skew-T-log-P diagrams using MetPy plotting software (May et al. 2008 - 2017) at Springfield, Misourri from 1200 UTC on 18 June to 1200 UTC on 19 June.

3. Results

a. Near Landfall

Figure 3 displays vertical profiles of Z_H, Z_{DR}, K_{DP}, ρ_{hv}, and drop size on 16 June over El Campo, TX as Tropical Storm Bill made landfall. Because the ρ_{hv} field provides information regarding hydrometeor diversity, regions of reduced ρ_{hv} can be used to detect the melting layer (e.g., Herzegh and Jameson 1992; Zrnic and Ryzhkov 1999; Ryzhkov et al. 2005b; Ryzhkov et al. 2005a; Kumjian 2013a). In this case the melting layer was located between 4.5-5 km, which is consistent with polarimetric radar observations of other landfalling tropical cyclones such as Hurricane Harvey in 2017 (Brauer et al. 2020). Values of Z_H ranged from 25-45 dBZ in the liquid phase after 1500 UTC, with the highest values occurring after 2000 UTC. Z_{DR} of 1-1.5 dB existed from 1500-1700 UTC, implying a slightly larger drop size when compared to the values of Z_{DR} of 0.5-1 dB that were observed later in the day after 1800 UTC. From the same 1500-1700 UTC period, values of K_{DP} were less than 0.25 degrees/km, whereas later in the day values ranged from 0.25-0.5 degrees/km. When combining the Z_H and Z_{DR} observations with K_{DP}, it can be seen that a small number concentration of larger drops existed from 1500-1700 UTC, whereas after 2000 UTC, there was a larger number concentration of smaller drops, consistent with tropical rainfall driven by CC (e.g., Squires 1956; Ulbrich and Atlas 2007; Carr et al. 2017). While the drop size appears to have increased towards the surface throughout the entire period (consistent with CC), the largest increase in drop size occurred after 2100 UTC on 16 June.

b. TCMI1: Southern Oklahoma

After Tropical Storm Bill progressed inland across north Texas and southern Oklahoma, it maintained its tropical precipitation characteristics. Figure 4 displays time-height curtains of the polarimetric radar variables and drop size at Grady, OK, which is near the time and location of TCMI1. The drop size was similar to that over El Campo, with values of Z_{DR} ranging from 1-1.5 dB in the liquid phase after 1800 UTC, and smaller values before this time. Similarly, values of K_{DP} of 0-0.25 degrees/km for the majority of the period, with higher values close to 0.5 degrees/km around 2200 UTC. At this time, Z_{DR} values were largest and Z_H was approximately 45 dBZ, implying that convection was responsible for the larger number concentration of larger drops. The ρ_{hv} field suggests that the melting layer height decreased slightly from the previous day over El Campo, ranging from 3.5-4.5 km, with an upward displacement during the period of convection at approximately 2200 UTC. This may be due to stronger updrafts inducing latent heat release which subsequently increased the height of the 0^oC isotherm. The drop size profile over Grady was similar to that over El Campo, with drop size that increased towards the surface below the melting layer, indicative of CC and warm rain. This can also be seen via Figure 5 which shows that the vertical distributions of Z_H and Z_{DR} over El Campo and Grady were consistent with low-echo centroid precipitation systems and are characterized by the majority of reflectivity remaining within the warm cloud layer (e.g., Vitale and Ryan 2013; Schroeder et al. 2016). Similarly, Z_{DR} also increased towards the surface at both locations below the melting layer which is indicative of CC. The Z_{DR} distribution was also shifted towards values between 0-1 dB, implying a small mean drop size at El Campo and Grady (e.g., Squires 1956; Ulbrich and Atlas 2007; Carr et al. 2017) Figure 5 also illustrates the frequency of K_{DP} and ρ_{hv} values with height at the same two locations. K_{DP} values from 0-0.5 degrees/km occurred below the melting layer at El Campo between 30-

40 different radar scans, indicating a large concentration of small drops (e.g., Brown et al. 2016; Didlake and Kumjian 2017; Brauer et al. 2020). Lastly, the high frequency of ρ_{hv} <0.98 between 4.5-5.5 km ASL implies mixed-phase precipitation and the approximate location of the melting layer.

Figure 6 shows along-track vertical profiles of reflectivity at Ku-band from the GPM DPR at 0538 UTC and 1454 UTC on 17 June. Although no additional overpass was available further north and east over Oklahoma, the 1454 UTC overpass provides a sense of the evolution of the reflectivity field as Bill progressed inland post-landfall. The DPR retrievals confirm the findings with the ground-based polarimetric radar observations. At 0538 UTC, a bright-band signature was evident at approximately 4.5-5 km, which is indicative of a melting layer at this altitude and is consistent with the 0^oC isotherm that was extracted from the GPM DPR. Below this level, the reflectivity increased towards the surface consistent with CC occurring within the warm cloud layer. Further, the retrieved D_M generally increases towards the surface, consistent with Porcacchia et al. (2019). As Bill tracked inland over north central Texas, the melting level was located slightly lower near 4.5 km, however there were upward displacements evident in the melting layer collocated with convection and associated values of reflectivity near 50 dBZ. Similarly, reflectivity predominantly increased below the melting layer, implying the maintenance of CC-dominant precipitation after Bill progressed hundreds of kilometers inland from the landfall point. Mean drop sizes (D_M) ranged from 0.75-1.5 mm, with higher values of 2 mm in regions of convection, Such observations were consistent with larger values seen in convection in other TCs such as Hurricane Harvey (2017) (Brauer et al. 2020; DeHart and Bell 2020). Finally, high drop number concentrations ($log_{10}(N_W)$) between 3-5 mm m^{-3} occurred during both times, with the highest values occurring in convective cores.

c. TCMI2: Southern Missouri, Illinois

As Bill continued to move north and east over southern Missouri, Illinois, and Kentucky from 19-20 June, the second TCMI occurred (TCMI2) at approximately 0000 UTC 20 June. Figures 7 and 8 show time-height curtains of Z_H, Z_{DR}, K_{DP}, ρ_{hv}, and drop size from the WSR-88D network at Cape Girardeau, MO and Cairo, IL on 19 June, respectively. Z_H values at the surface ranged from 30-40 dBZ after 2100 UTC at Cape Girardeau, with slightly lower values of 25-35 dBZ at Cairo, with distinctive bursts of weak convection after 1200 UTC, which explains the gaps in meteorological scatterers as $\rho_{hv} \leq 0.9$. Values of Z_{DR} were considerably lower than TCMI1, with values ranging from 0-1 dB at Cape Girardeau and 0-0.5 dB at Cairo, compared to 0.5-1.5 dB at El Campo and Grady. These lower values of Z_{DR} translate to a smaller drop size (e.g., Brown et al. 2016; Didlake and Kumjian 2017) and were likely due to CC or a balance between CC and drop breakup, as expected in a tropical environment (e.g., Kumjian and Prat 2014; Didlake and Kumjian 2017; Brauer et al. 2020). Additionally, signatures with an enhancement in hydrometeor number concentration in areas of weak convection (K_{DP} values near 0.25 degrees/km) occurred after 2100 UTC at both Cape Girardeau and Cairo. The vertical profiles of ρ_{hv} indicated that the melting layer height ranged from 4.0-5.5 km at both locations, and was located higher in altitude than Grady, OK.

Figure 9 illustrates the frequency of Z_H, Z_{DR}, K_{DP}, and ρ_{hv} with height at Cape Girardeau and Cairo to provide information regarding the dominant precipitation processes during TCMI2. From the framework used in Kumjian and Prat (2014), Carr et al. (2017), and Porcacchia et al. (2019), Z_H increased towards the surface while Z_{DR} decreased towards the surface below the melting layer at both locations. Such results indicate size-sorting and evaporation, which may be due to enhanced vertical wind shear, leading to more dry air entrainment into the core of Bill, which is known to disrupt the structure of tropical cyclones (e.g., Gray 1968; DeMaria and Kaplan 1994; Hanley et al. 2001; Corbosiero and Molinari 2002). Although size-sorting and evaporation were likely the dominant processes, the drop size distribution was still skewed towards a smaller drop size as Z_{DR} remained below 1 dB at both locations for the majority of the event. Similarly, echo tops associated with the weak convection were below 12 km ASL, and similar features are known to produce the most extreme rainfall rates rather than deep convection with high values of Z_H(Hamada et al. 2015). There were also instances where locations saw an enhancement in drop concentration as K_{DP} between 0.25-0.5 degrees/km were observed.

Although ground-based radar observations show evidence of size-sorting and evaporation being the dominant processes, retrievals from the GPM DPR during an overpass at 0436 UTC 20 June show evidence of CC or a balance between CC and drop breakup below the melting layer (Fig. 10). The melting layer was identified between 4 and 5 km on the cross-section of Ku-band reflectivity and denoted by the enhancement of reflectivity due to melting hydrometeors. Further, the 0^oC isotherm was also located at 5 km, indicating a deep warm cloud layer. Below this level, reflectivity increased from 25 dBZ to 35 dBZ at an along-track distance of 100 km, which is a signal of CC or a CC-breakup balance (Fig. 10b). D_M also increased from 0.75 to 1.2 mm at this location, with a larger mean drop size ranging from 1.25-1.75 mm within the weak convection (Fig. 10c). The vertical profiles of $log_{10}(N_W)$ show a drop concentration of 4.5 mm m^{-3} in the aforementioned region of CC, with slightly lower concentrations of 3.5-4.0 mm m^{-3} in the region of weak convection (Fig. 10d). The GPM DPR estimated a rainfall rate of 5-10 mm $hour^{-1}$ in the stratiform precipitation regions and enhanced rainfall rates of 20-35 mm $hour^{-1}$ in the embedded regions of weak convection (Fig. 10e). Lastly, Figure 10f shows regions of convection embedded in a broader region of stratiform precipitation. The aforementioned bright-band signature is likely a result of an area of stratiform precipitation within areas of weak convection.

d. Dynamics

While Bill certainly maintained tropical rainfall characteristics during TCMI2 over Southern Missouri and Illinois, the dynamics associated with Bill were investigated to determine how the large scale structure evolved during the re-intensification period. The primary feature of TCs is the presence of a low-level potential vorticity (PV) anomaly due to large amounts of latent heat release in convection (e.g., Möller and Smith 1994; Möller and Montgomery 2000; Trenberth and Fasullo 2007). This PV anomaly in TCs differs from extratropical cyclones, in which positive PV anomalies are typically found in the upper troposphere (e.g., Hoskins et al. 1985; Hoskins 2006). Figure 11 shows longitude-height cross-sections of PV and potential temperature at a constant latitude of 38^oN using the ERA-5 data from 2100 UTC 19 June to 1200 UTC 20 June during TCMI2 over Southern Illinois and Kentucky. Before the onset of TCMI2, the positive PV anomaly existed in the mid troposphere between 600-400 hPa, with a gradual lowering and intensification of the positive PV anomaly analyzed by 0300 UTC 20 June. By 0600 UTC 20 June, the positive PV anomaly was located in the lower-troposphere between 900-800 hPa, characteristic of low-level positive PV anomalies that are typically found in TCs.

Longitude-height cross-sections of vertical velocity and potential temperature were also plotted using the ERA-5 data along a constant latitude of 34^oN from 1200-2100 UTC 17 June (Fig. 12) during TCMI1, and along a constant latitude of 38^oN from 2100 UTC 19 June to 1200 UTC 20 June (Fig. 13) during TCMI2. Maximum ascent rates of 3 Pa s^{-1} occurred near 600 hPa during TCMI1, whereas maximum ascent rates were considerably stronger during TCMI2, nearing values of 5 Pa s^{-1}. Vertical velocity can be related to convective available potential energy (CAPE) (e.g., List and Lozowski 1970; Blanchard 1998), and the vertical distribution of CAPE can be directly related to updraft speed. Moist adiabatic profiles that are often frequently observed in tropical environments are characterized by ”skinny” CAPE profiles and are indicative of slow ascent rates (e.g., Davis 2001; Jessup and DeGaetano 2008; Vitale and Ryan 2013; Schroeder et al. 2016), whereas ”fat” CAPE profiles are associated with stronger updraft speeds and are more common in the midlatitudes. These weaker ascent rates are known to increase in-cloud residence time of hydrometeors, allowing for more efficient growth via CC (e.g., Vitale and Ryan 2013; Schroeder et al. 2016). In the case of Bill during TCMI1 and TCMI2, the magnitude of ascent was considerably less than vertical velocities captured in mid-latitude convection by ERA-5, which could be as high as 15 Pas^{-1} as was seen in a mid-latitude mesoscale convective system prior to Bill over the same region. The combination of low-echo centroid precipitation, shallow echo tops, and weak ascent rates further illustrates that Bill maintained tropical characteristics inland over southern Oklahoma, Missouri, southern Illinois, and Kentucky. Figure 14 shows observed soundings at Springfield, Missouri from 1200 UTC on 18 August to 1200 UTC on 19 August, which displays deep, moist adiabatic profiles and associated ”skinny” CAPE which characterized the environment of Bill as it progressed northeast over Missouri and Kentucky. It can also be seen that there is considerable speed and directional shear at all three times, perhaps explaining the dominant presence of size-sorting and evaporation as Bill moved over this region.

4. Discussion

Tropical cyclones that maintain their structure over land can cause flooding and damaging winds hundreds of kilometers from the landfall point (e.g., Arndt et al. 2009; Andersen and Shepherd 2014b). Tropical Storm Bill (2015) experienced two distinct TCMI events over (1) southern Oklahoma and (2) Missouri, southern Illinois, and Kentucky as it produced upwards of 400 mm of precipitation over this region from 16-20 June (Fig. 1). An important aspect of the inland maintenance of warm cloud microphysics and precipitation associated with tropical rainfall is that they are highly efficient processes to convert tropospheric water vapor to precipitation (i.e., precipitation efficiency). Further, these precipitation systems have a deep warm cloud layer (e.g., Davis 2001; Vitale and Ryan 2013; Schroeder et al. 2016; Brauer et al. 2020) dominated by CC or a CC-drop breakup balance and are known to account for excessive precipitation events in the mid-latitudes (e.g., Hisham Mohd Anip and Market 2007;Carr et al. 2017; Porcacchia et al. 2019). A novel aspect of TC Bill is that its TCMIs occurred during a period of available polarimetric radar observations from ground-based radars along with observations from the newly launched GPM DPR in 2014 (e.g., Hou et al. 2014; Skofronick-Jackson et al. 2017). Such datasets allowed for a more in-depth analysis and quantification of precipitation processes during the TCMI events that were not possible with prior events. These observational datasets can further benefit and improve the numerical modeling of landfalling TCs since, compared to radiation and PBL/surface schemes, microphysics schemes play the more critical role in the numerical model simulations of TCMIs (Yoo et al. 2020). Yoo et al. (2020) found that the TCMI of TC Kelvin was driven by moisture transport from the intertropical convergence zone, rather than latent heat fluxes from coupling to from warm, sandy soils. Thus, the inferred precipitation microphysics from the polarimetric radar observations and GPM DPR retrievals can be used to adjust the microphysical parameterization schemes accordingly in numerical simulations of TCMI to deliver model output that is more consistent with observations, and determine the role of precipitation microphysics of TCMI.

While inland over southern Oklahoma, Bill maintained dual-polarization radar signatures consistent with tropical rainfall and characterized by a large number concentration of small drops (Fig.4) (e.g., Squires 1956; Ulbrich and Atlas 2007; Xu et al. 2008; Brauer et al. 2020). Z_{DR} of 0.5-1.25 dB in addition to K_{DP} >0.5 degrees/km allows the classification of tropical rainfall, whereas Z_H alone is more sensitive to hydrometeor size (e.g., Austin 1987; Herzegh and Jameson 1992; Zrnic and Ryzhkov 1999; Kumjian 2013a). GPM DPR observations (Fig.6) during TCMI1 also showed an increase in drop size and Ku-band reflectivity below the melting layer, which is consistent with CC-dominant precipitation (e.g., Huang and Chen 2019; Porcacchia et al. 2019).

As Bill progressed inland over Missouri, southern Illinois, and Kentucky on 19-20 June, signatures of tropical precipitation were maintained during TCMI2, but were not as pronounced as when Bill was closer to the landfall point during TCMI1. Figure 9 illustrates signatures associated with evaporation and size-sorting as Z_H increased towards the surface and Z_{DR} decreased towards the surface (e.g., Kumjian and Prat 2014; Carr et al. 2017; Porcacchia et al. 2019). However, the values of Z_{DR} ranging from 0.5-1 dB, and K_{DP} as high as 0.25 degrees/km (Fig 7, Fig. 8) implies tropical rainfall characteristics similar to TCMI1 and shortly after the landfall point near El Campo, TX. The GPM DPR overpass over southern Illinois at 0436 UTC 20 June also identified Ku-band reflectivity and drop size increasing towards the surface, indicating CC-dominant precipitation or a balance between CC and drop breakup. These features are consistent with warm rain processes associated with tropical rainfall (Fig. 10). One possible reason for the occurrence of TCMI2 was the presence of anomalous mean latent heat fluxes of 105 Wm^{-2} over the region, with the land surface obtaining oceanic influences on the re-intensification of Bill (Wakefield et al. 2020).

5. Conclusions

The inland progression of Tropical Storm Bill over Texas and Oklahoma followed a two month period with record high precipitation throughout the region, which provided a unique opportunity to explore the microphysical evolution using polarimetric radar observations from the WSR-88D network and the GPM DPR. The exceptional precipitation during the 45 days prior to Bill resulted in anomalously high soil moisture and latent heat fluxes over the region, acting to increase boundary layer moisture and increase the warm cloud depth through latent heat release. As a result, Bill maintained tropical, warm rain characteristics as it tracked inland over southern Oklahoma and produced over 400 mm of rainfall in the aforementioned four day period during TCMI1. The polarimetric radar observations and GPM DPR measurements showed increasing reflectivity towards the surface below the melting layer, which is consistent with CC-dominant precipitation and/or a balance between CC and drop breakup. These signatures are consistent with tropical cyclone environments.

As Bill progressed inland over Missouri, southern Illinois, and Kentucky, an additional TCMI occurred. While dominant precipitation signatures were found to be associated with size-sorting and evaporation below the melting layer, there were still signatures of CC in the WSR-88D observations and the GPM DPR retrievals. Additionally, investigation of atmospheric dynamics during TCMI2 illustrates ascent rates that were similar to those in shallow, tropical convection, and low level positive PV anomalies indicative of low and mid-level latent heat release found in TCs. This further demonstrates that Bill maintained tropical characteristics from a dynamical framework several days post-landfall.

Limitations of this work include that the GPM DPR was only able to extract vertical profiles of reflectivity and drop size distribution moments at snapshots in time, limiting the extent in which a TCMI was observed from spaceborne radar. The echo top heights in the ground-based radar observations were also 2 km higher than the GPM DPR retrievals, which may be due to re-gridding of the WSR-88D data. Additional uncertainties arise with the ERA-5 reanalysis being unable to fully resolve the spatial details in the PV and vertical velocity fields, which may explain the vertical discontinuity in mid level PV as shown in Figure 12.

Future work should examine more places throughout the inland progression of Tropical Storm Bill as it moved into Missouri and northeastern Oklahoma to determine the temporal extent to which Bill maintained tropical rainfall characteristics. Additionally, it would be useful to compare this event to other less pronounced TCMI cases using the GPM DPR on a global scale and using ground-based radar measurements where available. Future analyses could also incorporate the use of disdrometer data to more precisely quantify the drop size distribution moments to compare to the GPM DPR algorithms that are used to estimate D_M and $log_{10}(N_W)$ from space. Another area that can be explored in future work are the impacts of latent heating on precipitation microphysics during periods of TCMI. Lastly, future research could perform a modeling study of the dynamics and thermodynamics associated with the TCMI periods to account for the uncertainties in the ERA-5 reanalysis.

Acknowledgements

Funding for this study was provided, in part by NASA Grant-80NSSC19K0681 and the NASA Modeling, Analysis, and Prediction (MAP) program (16-MAP16-013). This work was also supported by the Future Investigators in NASA Earth Space Science and Technology (FINNEST) award No. 80NSSC19K1365. We would also like to acknowledge Dr.David Considine and the generous support from the NASA MAP Program Grant No. 80NSSC17K0264. The authors thank the three anonymous reviewers that provided useful feedback and comments to improve the quality of this study. Additionally, the authors thank Jordan Christian, Melanie Schroers, Ryan Lagerquist, Tomer Burg, and Ty Dickinson for their valuable insight, guidance, and encouragement that was necessary to complete this work. The authors also thank Randy Chase and Steve Nesbitt at the University of Illinois Urbana-Champaign for providing source code used to complete this work.

Data Availability

The WSR-88D Level II polarimetric radar data used in this study can be accessed at `https://www.ncdc.noaa.gov/nexradinv/`. Due to agreements with research collaborators, the GridRad data used in this study cannot be made openly available. The GPM DPR data used in this work can be found at `https://search.earthdata.nasa.gov/search?fp=GPM&fi=DPR`. The ERA-5 reanalysis data set are openly available at `https://cds.climate.copernicus.eu/cdsapp#!/dataset/reanalysis-era5-pressure-levels?tab=form`, and the upper-air data that were used in this study can be accessed via `http://weather.uwyo.edu/upperair/sounding.html`.

References

Andersen, T. K., and J. M. Shepherd, 2014a: A global spatiotemporal analysis of inland tropical cyclone maintenance or intensification. *International Journal of Climatology*, **34 (2)**, 391–402, doi:10.1002/joc.3693.

Andersen, T. K., and J. M. Shepherd, 2014b: A global spatiotemporal analysis of inland tropical cyclone maintenance or intensification. *International Journal of Climatology*, **34 (2)**, 391–402, doi:10.1002/joc.3693.

Arndt, D. S., J. B. Basara, R. A. McPherson, B. G. Illston, G. D. McManus, and D. B. Demko, 2009: Observations of the overland reintensification of tropical storm erin (2007). *Bulletin of the American Meteorological Society*, **90 (8)**, 1079–1094, doi:10.1175/2009BAMS2644.1.

Austin, P. M., 1987: Relation between measured radar reflectivity and surface rainfall. *Monthly Weather Review*, **115 (5)**, 1053–1070, doi:10.1175/1520-0493(1987)115⟨1053:RBMRRA⟩2.0.CO;2.

Bechini, R., L. Baldini, R. Cremonini, and E. Gorgucci, 2008: Differential reflectivity calibration for operational radars. *Journal of Atmospheric and Oceanic Technology*, **25 (9)**, 1542–1555, doi:10.1175/2008JTECHA1037.1.

Blanchard, D. O., 1998: Assessing the vertical distribution of convective available potential energy. *Weather and Forecasting*, **13 (3)**, 870–877, doi:10.1175/1520-0434(1998)013⟨0870:ATVDOC⟩2.0.CO;2.

Bowman, K. P., and C. R. Homeyer, 2017: GridRad - Three-Dimensional Gridded NEXRAD WSR-88D Radar Data. Research Data Archive at the National Center for Atmospheric Research, Computational and Information Systems Laboratory, Boulder CO.

Brauer, N. S., J. B. Basara, C. R. Homeyer, G. M. McFarquhar, and P. E. Kirstetter, 2020: Quantifying Precipitation Efficiency and Drivers of Excessive Precipitation in Post-Landfall Hurricane Harvey. *Journal of Hydrometeorology*, **21 (3)**, 433–452, doi:10.1175/JHM-D-19-0192.1.

Bringi, V. N., V. Chandrasekar, N. Balakrishnan, and D. S. Zrnić, 1990: An examination of propagation effects in rainfall on radar measurements at microwave frequencies. *Journal of Atmospheric and Oceanic Technology*, **7 (6)**, 829–840, doi:10.1175/1520-0426(1990)007⟨0829:AEOPEI⟩2.0.CO;2.

Brock, F. V., K. C. Crawford, R. L. Elliott, G. W. Cuperus, S. J. Stadler, H. L. Johnson, and M. D. Eilts, 1995: The Oklahoma Mesonet: A Technical Overview. *Journal of Atmospheric and Oceanic Technology*, **12 (1)**, 5–19, doi:10.1175/1520-0426(1995)012⟨0005:TOMATO⟩2.0.CO;2.

Brown, B. R., M. M. Bell, and A. J. Frambach, 2016: Validation of simulated hurricane drop size distributions using polarimetric radar. *Geophysical Research Letters*, **43 (2)**, 910–917, doi:10.1002/2015GL067278.

Cao, Q., G. Zhang, E. Brandes, T. Schuur, A. Ryzhkov, and K. Ikeda, 2008: Analysis of video disdrometer and polarimetric radar data to characterize rain microphysics in oklahoma. *Journal* *of Applied Meteorology and Climatology*, **47 (8)**, 2238–2255, doi:10.1175/2008JAMC1732.1.

Carr, N., P. E. Kirstetter, J. J. Gourley, and Y. Hong, 2017: Polarimetric signatures of midlatitude warm-rain precipitation events. *Journal of Applied Meteorology and Climatology*, **56 (3)**, 697–711, doi:10.1175/JAMC-D-16-0164.1.

Cifelli, R., V. Chandrasekar, S. Lim, P. C. Kennedy, Y. Wang, and S. A. Rutledge, 2011: A new dual-polarization radar rainfall algorithm: Application in colorado precipitation events. *Journal of Atmospheric and Oceanic Technology*, **28 (3)**, 352–364, doi:10.1175/2010JTECHA1488.1.

Clark, C. A., and P. W. Arritt, 1995: Numerical simulations of the effect of soil moisture and vegetation cover on the development of deep convection. *Journal of Applied Meteorology*, **34 (9)**, 2029–2045, doi:10.1175/1520-0450(1995)034⟨2029:NSOTEO⟩2.0.CO;2.

Corbosiero, K. L., and J. Molinari, 2002: The Effects of Vertical Wind Shear on the Distribution of Convection in Tropical Cyclones. *Monthly Weather Review*, **130 (8)**, 2110–2123, doi:10.1175/1520-0493(2002)130⟨2110:TEOVWS⟩2.0.CO;2.

Crum, T. D., and R. L. Alberty, 1993: The WSR-88D and the WSR-88D Operational Support Facility. *Bulletin of the American Meteorological Society*, **74 (9)**, 1669–1688, doi:10.1175/1520-0477(1993)074⟨1669:TWATWO⟩2.0.CO;2.

Daly, C., R. P. Neilson, and D. L. Phillips, 1994: A statistical-topographic model for mapping climatological precipitation over mountainous terrain. *Journal of Applied Meteorology*, **33 (2)**, 140–158, doi:10.1175/1520-0450(1994)033⟨0140:ASTMFM⟩2.0.CO;2.

Davis, R. S., 2001: Flash flood forecast and detection methods. *Meteorological Monographs*, **50**, 481–526, doi:10.1175/0065-9401-28.50.481.

DeHart, J. C., and M. M. Bell, 2020: A comparison of the polarimetric radar characteristics of heavy rainfall from hurricanes harvey (2017) and florence (2018). *Journal of Geophysical Research: Atmospheres*, **125 (11)**, e2019JD032 212, doi:10.1029/2019JD032212.

DeMaria, M., and J. Kaplan, 1994: A Statistical Hurricane Intensity Prediction Scheme (SHIPS) for the Atlantic Basin. *Weather and Forecasting*, **9 (2)**, 209–220, doi:10.1175/1520-0434(1994)009⟨0209:ASHIPS⟩2.0.CO;2.

Didlake, A. C., and M. R. Kumjian, 2017: Examining polarimetric radar observations of bulk microphysical structures and their relation to vortex kinematics in hurricane arthur (2014). *Monthly Weather Review*, **145 (11)**, 4521–4541, doi:10.1175/MWR-D-17-0035.1.

Didlake Jr., A. C., and M. R. Kumjian, 2018: Examining storm asymmetries in hurricane irma (2017) using polarimetric radar observations. *Geophysical Research Letters*, **45 (24)**, 13,513–13,522, doi:10.1029/2018GL080739.

Duchon, C. E., C. A. Fiebrich, and B. G. Illston, 2017: Observing the May 2015 Record Rainfall at Norman, Oklahoma, Using Various Methods. *Journal of Hydrometeorology*, **18 (11)**, 3043–3049, doi:10.1175/JHM-D-17-0137.1.

Emanuel, K., J. Callaghan, and P. Otto, 2008: A hypothesis for the redevelopment of warm-core cyclones over northern australia. *Monthly Weather Review*, **136 (10)**, 3863–3872, doi:10.1175/2008MWR2409.1.

Evans, C., R. S. Schumacher, and T. J. Galarneau, 2011: Sensitivity in the overland reintensification of tropical cyclone erin (2007) to near-surface soil moisture characteristics. *Monthly Weather Review*, **139 (12)**, 3848–3870, doi:10.1175/2011MWR3593.1.

Feng, Y.-C., and M. M. Bell, 2019: Microphysical characteristics of an asymmetric eyewall in major hurricane harvey (2017). *Geophysical Research Letters*, **46 (1)**, 461–471, doi:10.1029/2018GL080770.

Giangrande, S. E., and A. V. Ryzhkov, 2008: Estimation of rainfall based on the results of polarimetric echo classification. *Journal of Applied Meteorology and Climatology*, **47 (9)**, 2445–2462, doi:10.1175/2008JAMC1753.1.

Gorgucci, E., V. Chandrasekar, V. N. Bringi, and G. Scarchilli, 2002: Estimation of raindrop size distribution parameters from polarimetric radar measurements. *Journal of the Atmospheric Sciences*, **59 (15)**, 2373–2384, doi:10.1175/1520-0469(2002)059⟨2373:EORSDP⟩2.0.CO;2.

Gorgucci, E., G. Scarchilli, and V. Chandrasekar, 1992: Calibration of radars using polarimetric techniques. *Geoscience and Remote Sensing, IEEE Transactions on*, **30**, 853 – 858, doi:10.1109/36.175319.

Grams, H. M., J. Zhang, and K. L. Elmore, 2014: Automated identification of enhanced rainfall rates using the near-storm environment for radar precipitation estimates. *Journal of Hydrometeorology*, **15 (3)**, 1238–1254, doi:10.1175/JHM-D-13-042.1.

Gray, W., I. Cluckie, and R. Griffith, 2006: Aspects of melting and the radar bright band. *Meteorological Applications*, **8**, 371 – 379, doi:10.1017/S1350482701003139.

Gray, W. M., 1968: Global View of Region Origin of Tropical Disturbances and Storms. *Monthly Weather Review*, **96 (10)**, 669–700, doi:10.1175/1520-0493(1968)096⟨0669:GVOTOO⟩2.0.CO;2.

Griffin, E. M., T. J. Schuur, D. R. MacGorman, M. R. Kumjian, and A. O. Fierro, 2014: An electrical and polarimetric analysis of the overland reintensification of tropical storm erin (2007). *Monthly Weather Review*, **142 (6)**, 2321–2344, doi:10.1175/MWR-D-13-00360.1.

Guo, Z., and Coauthors, 2006: Glace: The global land–atmosphere coupling experiment. part ii: Analysis. *Journal of Hydrometeorology*, **7 (4)**, 611–625, doi:10.1175/JHM511.1.

Hamada, A., Y. N. Takayabu, C. Liu, and E. J. Zipser, 2015: Weak linkage between the heaviest rainfall and tallest storms. *Nature Communications*, **6 (1)**, 6213, doi:10.1038/ncomms7213.

Hanley, D., J. Molinari, and D. Keyser, 2001: A Composite Study of the Interactions between Tropical Cyclones and Upper-Tropospheric Troughs. *Monthly Weather Review*, **129 (10)**, 2570–2584, doi:10.1175/1520-0493(2001)129⟨2570:ACSOTI⟩2.0.CO;2.

Hersbach, H., and Coauthors, 2019: Global reanalysis: goodbye ERA-Interim, hello ERA5. 17–24, doi:10.21957/vf291hehd7, URL https://www.ecmwf.int/node/19027.

Herzegh, P. H., and A. R. Jameson, 1992: Observing precipitation through dual-polarization radar measurements. *Bulletin of the American Meteorological Society*, **73 (9)**, 1365–1376, doi:10.1175/1520-0477(1992)073⟨1365:OPTDPR⟩2.0.CO;2.

Hisham Mohd Anip, M., and P. Market, 2007: Dominant factors influencing precipitation efficiency in a continental mid-latitude location. *Tellus A*, doi:{10.3402/tellusa.v59i1.14853}.

Hoskins, B., 2006: A potential vorticity view of synoptic development. *Meteorological Applications*, **4**, 325 – 334, doi:10.1017/S1350482797000716.

Hoskins, B. J., M. E. McIntyre, and A. W. Robertson, 1985: On the use and significance of isentropic potential vorticity maps. *Quarterly Journal of the Royal Meteorological Society*, **111 (470)**, 877–946, doi:10.1002/qj.49711147002.

Hou, A. Y., and Coauthors, 2014: The global precipitation measurement mission. *Bulletin of the American Meteorological Society*, **95 (5)**, 701–722, doi:10.1175/BAMS-D-13-00164.1.

Huang, H., and F. Chen, 2019: Precipitation microphysics of tropical cyclones over the western north pacific based on gpm dpr observations: A preliminary analysis. *Journal of Geophysical Research: Atmospheres*, **124 (6)**, 3124–3142, doi:10.1029/2018JD029454.

Jameson, A. R., 1985: Microphysical Interpretation of Multiparameter Radar Measurements in Rain. Part III: Interpretation and Measurement of Propagation Differential Phase Shift between Orthogonal Linear Polarizations. *Journal of the Atmospheric Sciences*, **42 (6)**, 607–614, doi: 10.1175/1520-0469(1985)042⟨0607:MIOMRM⟩2.0.CO;2.

Jarrell, J. D., M. Mayfield, E. N. Rappaport, and C. Landsea, 2001: The deadliest, costliest, and most intense united states hurricanes from 1900 to 2000. *NOAA Technical Memorandum*, doi: https://www.nhc.noaa.gov/pdf/NWS-TPC-2001-3.pdf.

Jessup, S. M., and A. T. DeGaetano, 2008: A Statistical Comparison of the Properties of Flash Flooding and Nonflooding Precipitation Events in Portions of New York and Pennsylvania. *Weather and Forecasting*, **23 (1)**, 114–130, doi:10.1175/2007WAF2006066.1.

Kellner, O., D. Niyogi, M. Lei, and A. Kumar, 2011: The role of anomalous soil moisture on the inland reintensification of tropical storm erin (2007). *Natural Hazards*, **63**, doi:10.1007/s11069-011-9966-6.

Kirstetter, P.-E., H. Andrieu, B. Boudevillain, and G. Delrieu, 2013: A physically based identification of vertical profiles of reflectivity from volume scan radar data. *Journal of Applied Meteorology and Climatology*, **52 (7)**, 1645–1663, doi:10.1175/JAMC-D-12-0228.1.

Koster, R. D., and Coauthors, 2006: Glace: The global land–atmosphere coupling experiment. part i: Overview. *Journal of Hydrometeorology*, **7 (4)**, 590–610, doi:10.1175/JHM510.1.

Koster, R. D., and Coauthors, 2011: The second phase of the global land–atmosphere coupling experiment: Soil moisture contributions to subseasonal forecast skill. *Journal of Hydrometeorology*, **12 (5)**, 805–822, doi:10.1175/2011JHM1365.1.

Kozu, T., and Coauthors, 2001: Development of precipitation radar onboard the tropical rainfall measuring mission (trmm) satellite. *Geoscience and Remote Sensing, IEEE Transactions on*, **39**, 102 – 116, doi:10.1109/36.898669.

Kumjian, M., 2013a: Principles and Applications of Dual-Polarization Weather Radar. Part I: Description of the Polarimetric Radar Variables. *Journal of Operational Meteorology*, **1**, 226–242, doi:10.15191/nwajom.2013.0119.

Kumjian, M., 2013b: Principles and applications of dual-polarization weather radar. part ii: Warm- and cold-season applications. *Journal of Operational Meteorology*, **1**, 243–264, doi:10.15191/nwajom.2013.0120.

Kumjian, M. R., and O. P. Prat, 2014: The impact of raindrop collisional processes on the polarimetric radar variables. *Journal of the Atmospheric Sciences*, **71 (8)**, 3052–3067, doi:10.1175/JAS-D-13-0357.1.

List, R., and E. P. Lozowski, 1970: Pressure perturbations and buoyancy in convective clouds. *Journal of the Atmospheric Sciences*, **27 (1)**, 168–170, doi:10.1175/1520-0469(1970)027⟨0168:PPABIC⟩2.0.CO;2.

Lynn, B. H., W.-K. Tao, and P. J. Wetzel, 1998: A study of landscape-generated deep moist convection. *Monthly Weather Review*, **126 (4)**, 928–942, doi:10.1175/1520-0493(1998)126⟨0928:ASOLGD⟩2.0.CO;2.

May, R., S. Arms, P. Marsh, E. Bruning, and J. Leeman, 2008 - 2017: Metpy: A Python package for meteorological data. Boulder, Colorado, doi:10.5065/D6WW7G29.

McPherson, R. A., and Coauthors, 2007: Statewide Monitoring of the Mesoscale Environment: A Technical Update on the Oklahoma Mesonet. *Journal of Atmospheric and Oceanic Technology*, **24 (3)**, 301–321, doi:10.1175/JTECH1976.1.

Medlin, J. M., S. K. Kimball, and K. G. Blackwell, 2007: Radar and rain gauge analysis of the extreme rainfall during hurricane danny's (1997) landfall. *Monthly Weather Review*, **135 (5)**, 1869–1888, doi:10.1175/MWR3368.1.

Monteverdi, J., and R. Edwards, 2010: The redevelopment of a warm core structure in erin: A case of inland tropical storm formation. *Electronic Journal of Severe Storms Meteorology*, **5**, 1–18.

Möller, J. D., and M. T. Montgomery, 2000: Tropical cyclone evolution via potential vorticity anomalies in a three-dimensional balance model. *Journal of the Atmospheric Sciences*, **57 (20)**, 3366–3387, doi:10.1175/1520-0469(2000)057⟨3366:TCEVPV⟩2.0.CO;2.

Möller, J. D., and R. K. Smith, 1994: The development of potential vorticity in a hurricane-like vortex. *Quarterly Journal of the Royal Meteorological Society*, **120 (519)**, 1255–1265, doi:10.1002/qj.49712051907.

Nair, U., and Coauthors, 2019: Influence of land cover and soil moisture based brown ocean effect on an extreme rainfall event from a louisiana gulf coast tropical system. *Scientific Reports*, **9**, 17 136, doi:10.1038/s41598-019-53031-6.

NOAA National Weather Service (NWS) Radar Operations Center, 1991: NOAA Next Generation Radar (NEXRAD) Level 2 Base Data. NOAA National Centers for Environmental Information, doi:doi:10.7289/V5W9574V.

Porcacchia, L., P.-E. Kirstetter, V. Maggioni, and S. Tanelli, 2019: Investigating the gpm dual-frequency precipitation radar signatures of low-level precipitation enhancement. *Quarterly Journal of the Royal Meteorological Society*, **145 (724)**, 3161–3174, doi:10.1002/qj.3611.

Rappaport, E. N., 2000: Loss of life in the united states associated with recent atlantic tropical cyclones. *Bulletin of the American Meteorological Society*, **81 (9)**, 2065–2074, doi:10.1175/1520-0477(2000)081⟨2065:LOLITU⟩2.3.CO;2.

Ryzhkov, A., P. Zhang, H. Reeves, M. Kumjian, T. Tschallener, S. Trömel, and C. Simmer, 2016: Quasi-vertical profiles—a new way to look at polarimetric radar data. *Journal of Atmospheric and Oceanic Technology*, **33 (3)**, 551–562, doi:10.1175/JTECH-D-15-0020.1.

Ryzhkov, A. V., 2007: The impact of beam broadening on the quality of radar polarimetric data. *Journal of Atmospheric and Oceanic Technology*, **24 (5)**, 729–744, doi:10.1175/JTECH2003.1.

Ryzhkov, A. V., S. E. Giangrande, and T. J. Schuur, 2005a: Rainfall estimation with a polarimetric prototype of wsr-88d. *Journal of Applied Meteorology*, **44 (4)**, 502–515, doi:10.1175/JAM2213.1.

Ryzhkov, A. V., T. J. Schuur, D. W. Burgess, P. L. Heinselman, S. E. Giangrande, and D. S. Zrnic, 2005b: The joint polarization experiment: Polarimetric rainfall measurements and hydrometeor classification. *Bulletin of the American Meteorological Society*, **86 (6)**, 809–824, doi:10.1175/BAMS-86-6-809.

Schroeder, A., J. Basara, J. M. Shepherd, and S. Nelson, 2016: Insights into Atmospheric Contributors to Urban Flash Flooding across the United States Using an Analysis of Rawinsonde Data and Associated Calculated Parameters. *Journal of Applied Meteorology and Climatology*, **55 (2)**, 313–323, doi:10.1175/JAMC-D-14-0232.1.

Science Applications International Corporation and National Hurricane Center, 1993: Global Tropical Cyclone ”Best Track” Position and Intensity Data. Research Data Archive at the National Center for Atmospheric Research, Computational and Information Systems Laboratory, Boulder CO, URL http://rda.ucar.edu/datasets/ds824.1/.

Seliga, T. A., and V. N. Bringi, 1976: Potential use of radar differential reflectivity measurements at orthogonal polarizations for measuring precipitation. *Journal of Applied Meteorology*, **15 (1)**, 69–76, doi:10.1175/1520-0450(1976)015⟨0069:PUORDR⟩2.0.CO;2.

Seliga, T. A., and V. N. Bringi, 1978: Differential reflectivity and differential phase shift: Applications in radar meteorology. *Radio Science*, **13 (2)**, 271–275, doi:10.1029/RS013i002p00271.

Skofronick-Jackson, G., and Coauthors, 2017: The global precipitation measurement (gpm) mission for science and society. *Bulletin of the American Meteorological Society*, **98 (8)**, 1679–1695, doi:10.1175/BAMS-D-15-00306.1.

Smalley, M., P.-E. Kirstetter, and T. L’Ecuyer, 2017: How frequent is precipitation over the contiguous united states? perspectives from ground-based and spaceborne radars. *Journal of Hydrometeorology*, **18 (6)**, 1657–1672, doi:10.1175/JHM-D-16-0242.1.

Squires, P., 1956: The Micro-Structure of Cumuli in Maritime and Continental Air. *Tellus*, **8 (4)**, 443.

Testud, J., E. Le Bouar, E. Obligis, and M. Ali-Mehenni, 2000: The rain profiling algorithm applied to polarimetric weather radar. *Journal of Atmospheric and Oceanic Technology*, **17 (3)**, 332–356, doi:10.1175/1520-0426(2000)017⟨0332:TRPAAT⟩2.0.CO;2.

Trenberth, K. E., and J. Fasullo, 2007: Water and energy budgets of hurricanes and implications for climate change. *Journal of Geophysical Research: Atmospheres*, **112 (D23)**, doi:10.1029/2006JD008304.

Ulbrich, C., and D. Atlas, 2007: Microphysics of raindrop size spectra: Tropical continental and maritime storms. *Journal of Applied Meteorology and Climatology - J APPL METEOROL CLIMATOL*, **46**, 1777–1791, doi:10.1175/2007JAMC1649.1.

Vitale, J., and T. Ryan, 2013: Operational recognition of high precipitation efficiency and low-echo-centroid convection. *Journal of Operational Meteorology*, **1**, 128–143, doi:10.15191/nwajom.2013.0112.

Wang, Y., and V. Chandrasekar, 2009: Algorithm for Estimation of the Specific Differential Phase. *Journal of Atmospheric and Oceanic Technology*, **26 (12)**, 2565–2578, doi:10.1175/2009JTECHA1358.1.

Wei, J., H. Su, and Z.-L. Yang, 2015: Impact of moisture flux convergence and soil moisture on precipitation: A case study for the southern united states with implications for the globe. *Climate Dynamics*, **46**, doi:10.1007/s00382-015-2593-2.

Xu, X., K. Howard, and J. Zhang, 2008: An automated radar technique for the identification of tropical precipitation. *Journal of Hydrometeorology*, **9 (5)**, 885–902, doi:10.1175/2007JHM954.1.

Yoo, J., J. A. Santanello, M. Shepherd, S. Kumar, P. Lawston, and A. M. Thomas, 2020: Quantification of the land surface and brown ocean influence on tropical cyclone intensification over land. *Journal of Hydrometeorology*, **21 (6)**, 1171–1192, doi:10.1175/JHM-D-19-0214.1.

Zhang, P., D. Zrnić, and A. Ryzhkov, 2013: Partial beam blockage correction using polarimetric radar measurements. *Journal of Atmospheric and Oceanic Technology*, **30 (5)**, 861–872, doi:10.1175/JTECH-D-12-00075.1.

Zrnic, D. S., and A. V. Ryzhkov, 1999: Polarimetry for weather surveillance radars. *Bulletin of the American Meteorological Society*, **80 (3)**, 389–406, doi:10.1175/1520-0477(1999)080⟨0389:PFWSR⟩2.0.CO;2.

Zrnić, D. S., and A. Ryzhkov, 1996: Advantages of rain measurements using specific differential phase. *Journal of Atmospheric and Oceanic Technology*, **13 (2)**, 454–464, doi:10.1175/1520-0426(1996)013⟨0454:AORMUS⟩2.0.CO;2.

LIST OF FIGURES

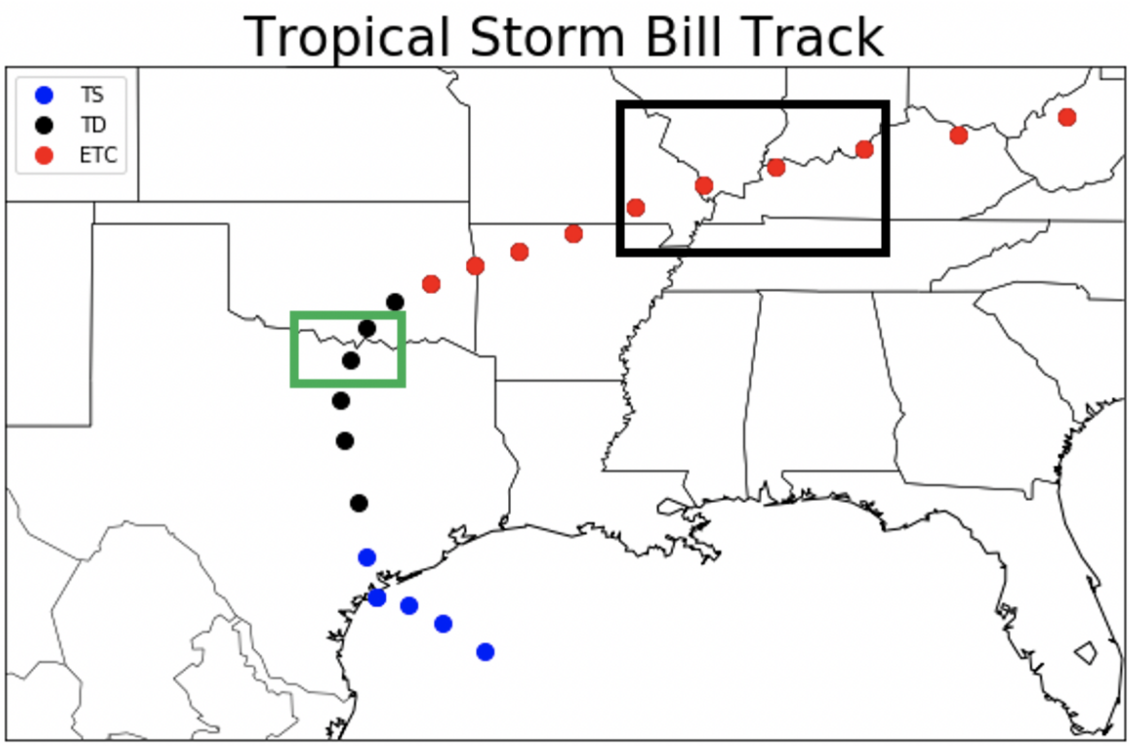

FIG. 1. Hurricane Database (HURDAT2) Best Track plot of Tropical Storm Bill from 16-21 June, 2015. Each point is spaced apart in 6-hour time increments. The green box represents the location of TCMI1 from 1200-1800 UTC 17 June, and the black box represents the location of TCMI2 from 1200 UTC 19 June to 1200 UTC 20 June.

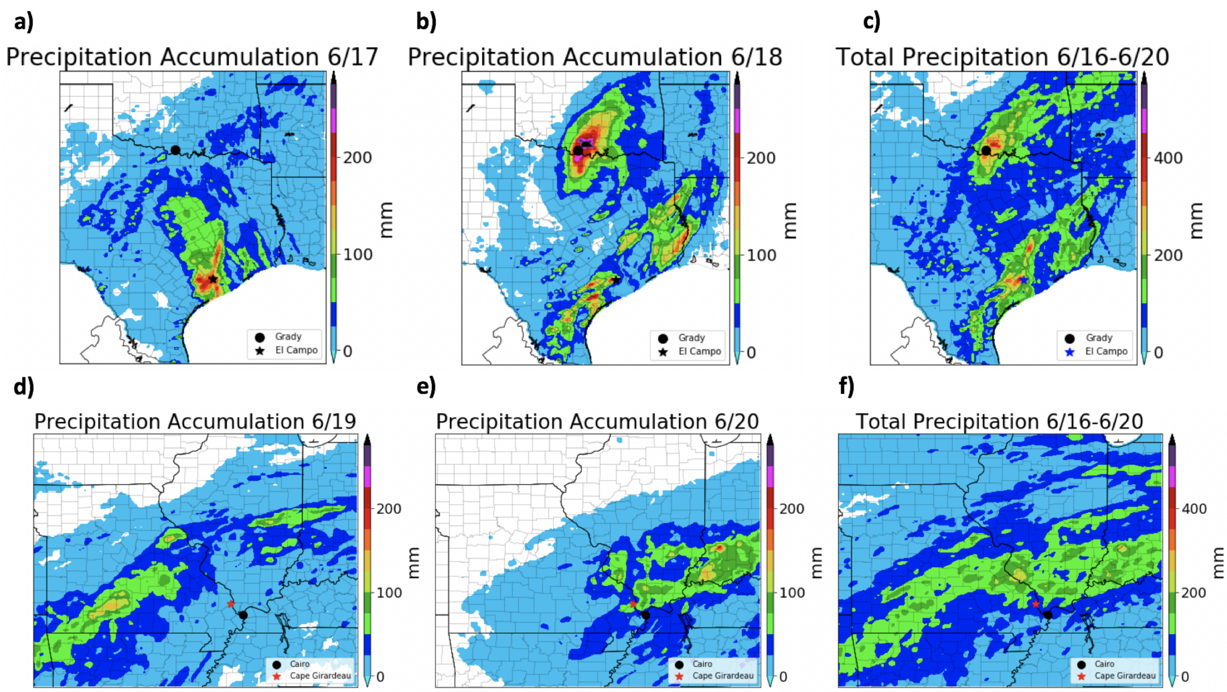

FIG. 2. PRISM daily accumulated precipitation over Texas and Oklahoma from 16-17 June (a. and b.), total accumulated precipitation from 16-20 June (c.), daily accumulated precipitation over Missouri and Illinois from 19-20 June (d. and e.), and total accumulated precipitation from 16-20 June (f.).

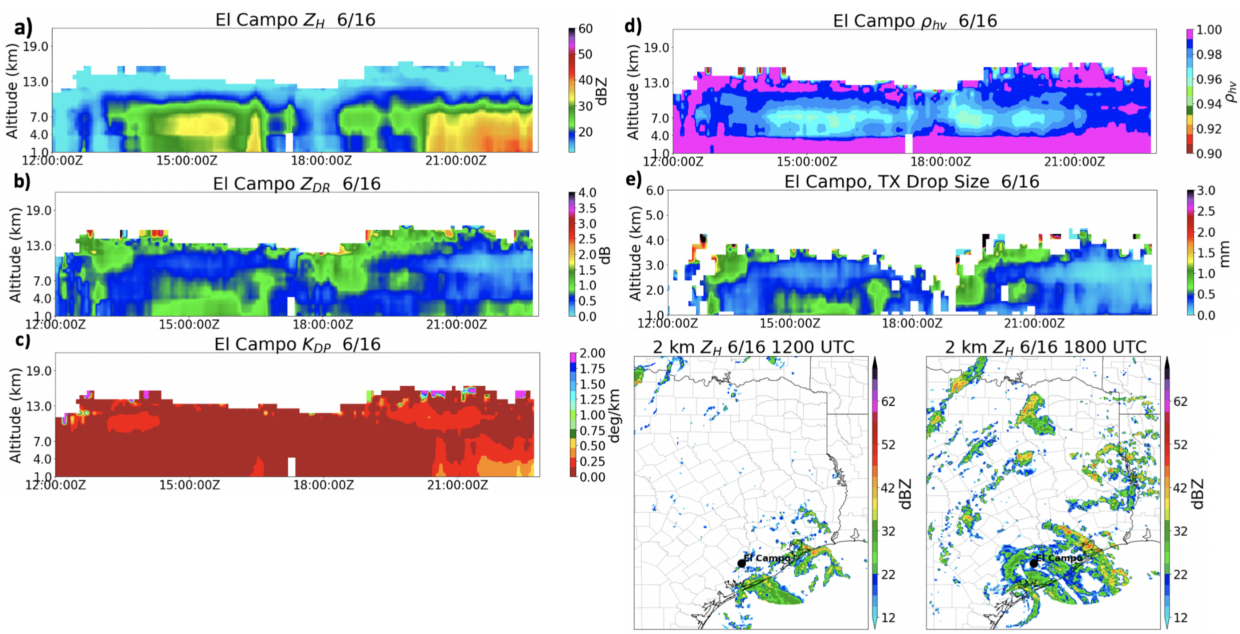

812 FIG. 3. Time-height curtains of Z_H (a), Z_{DR} (b), K_{DP} (c), ρ_{hv} (d), and drop size (e) near the landfall point over
813 El Campo, TX on from 1200 UTC 16 June-0000 UTC 17 June, and images of 2 km Z_H at 1200 UTC and 1800
814 UTC 16 June.

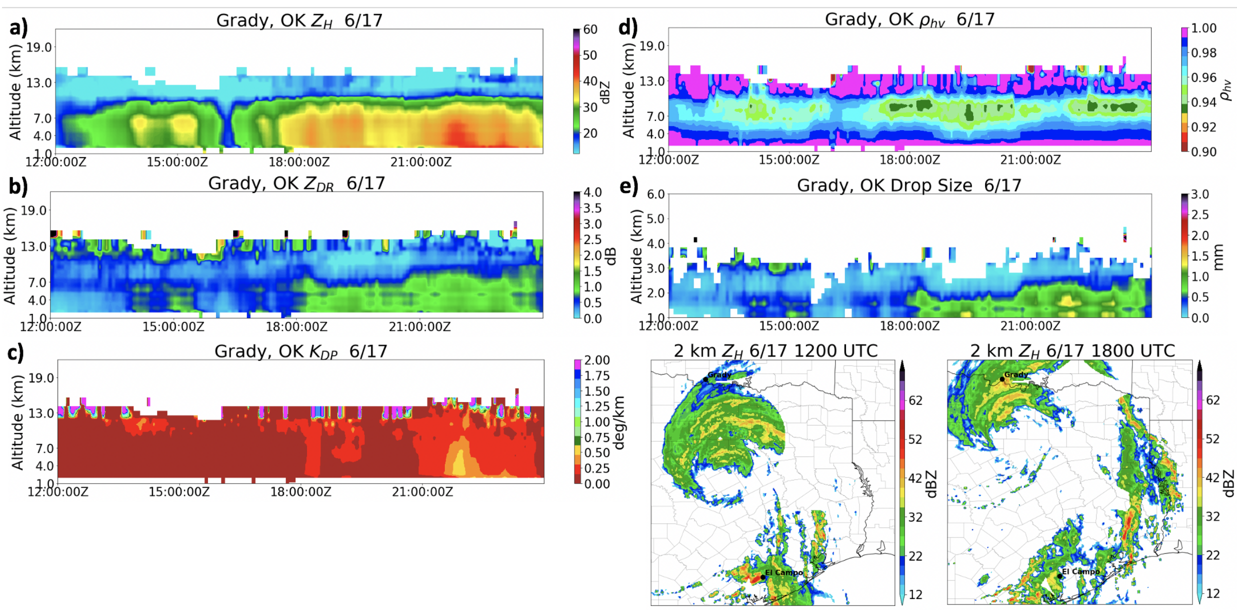

815 FIG. 4. Time-height curtains of Z_H (a), Z_{DR} (b), K_{DP} (c), ρ_{hv} (d), and drop size (e) during TCMI1 over Grady,
816 OK on from 1200 UTC 17 June-0000 UTC 18 June, and images of 2 km Z_H at 1200 UTC and 1800 UTC 17
817 June.

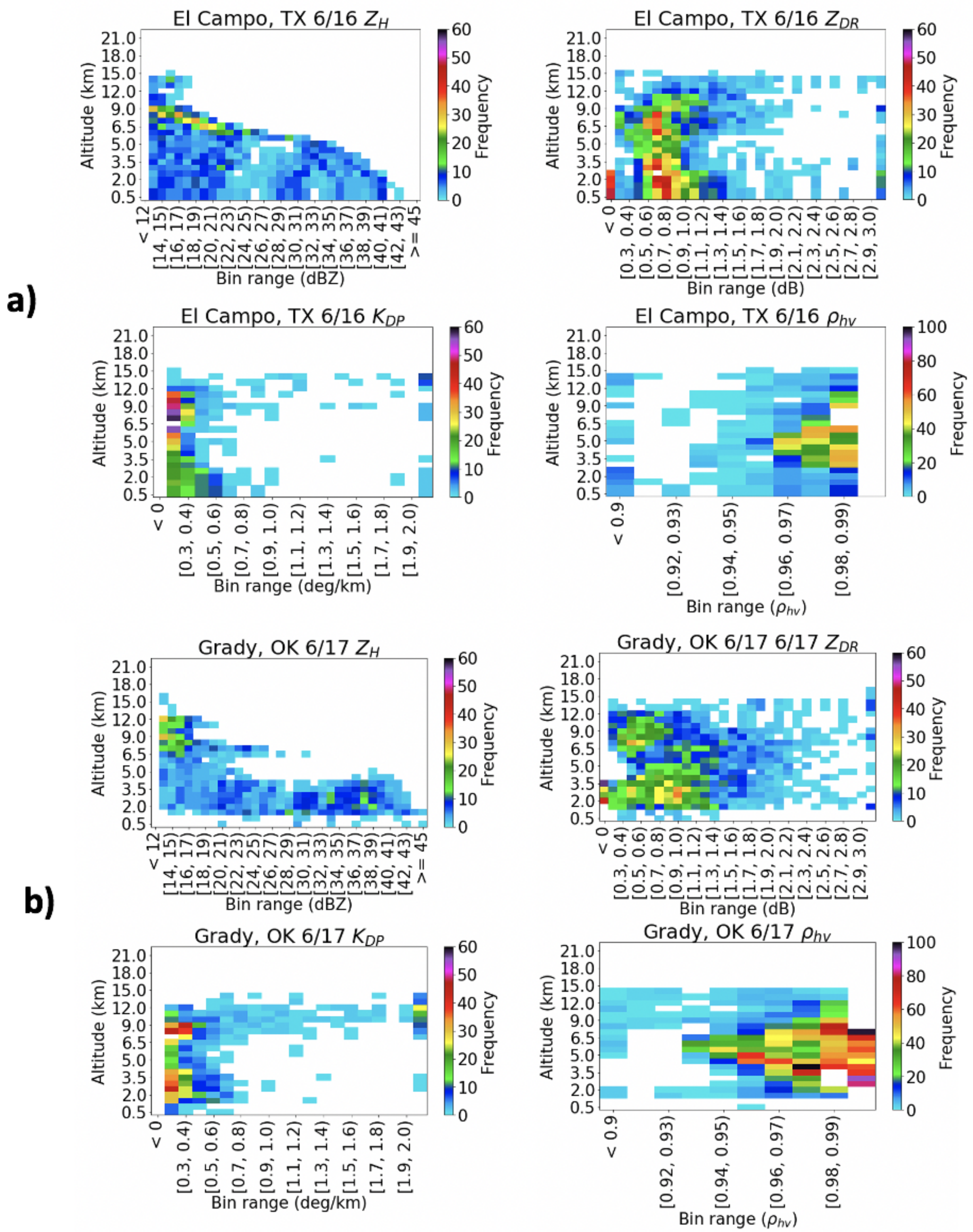

FIG. 5. Contoured Frequency By Altitude Diagrams (CFADs) of Z_H Z_{DR}, K_{DP}, and ρ_{hv} at El Campo, TX on 16 June (a), and Grady, OK on 17 June during TCMI1 (b).

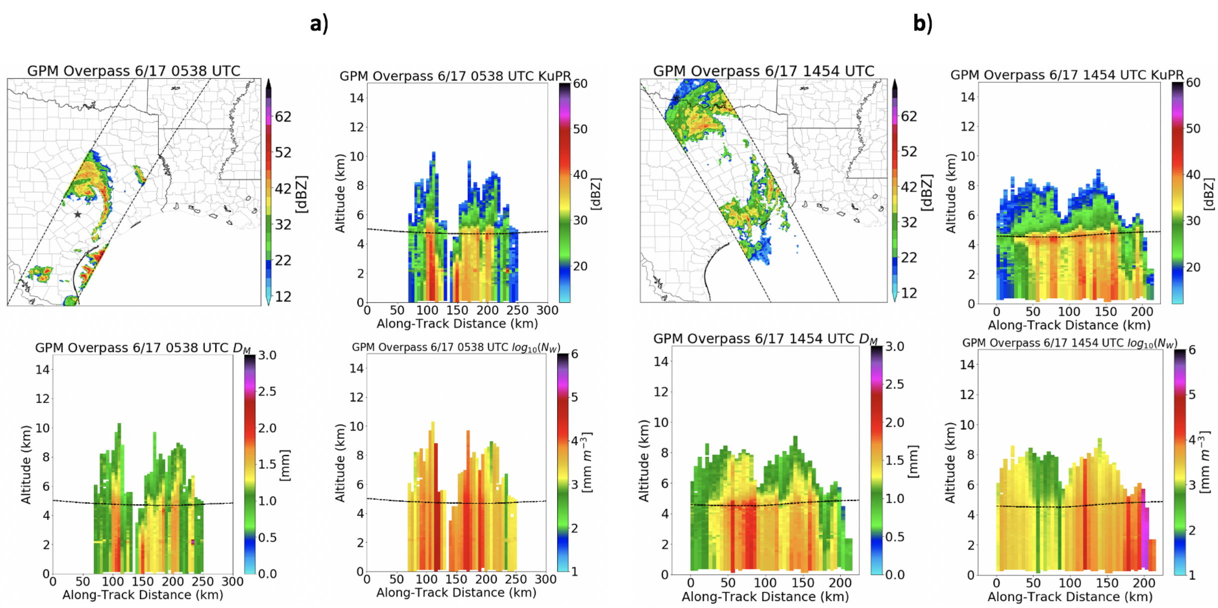

FIG. 6. GPM DPR along-track vertical profiles of $Z_M(Ku)$, D_M, and $log_{10}(N_W)$ at 0538 UTC (a) and 1454 UTC (b) on 17 June, 2015 over Texas. The dashed line represents the 0^oC isotherm.

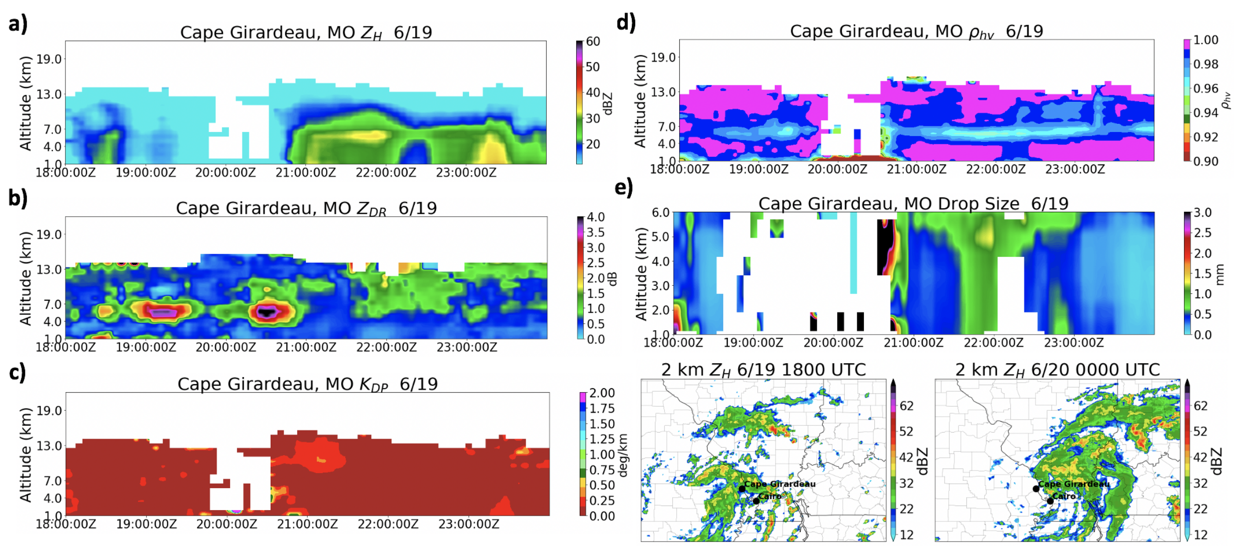

FIG. 7. Time-height curtains of Z_H (a), Z_{DR} (b), K_{DP} (c), ρ_{hv} (d), and drop size (e) during TCMI2 over Cape Girardeau, MO on from 1800 UTC 19 June-0000 UTC 20 June, and images of 2 km Z_H at 1800 UTC 19 June and 0000 UTC 20 June.

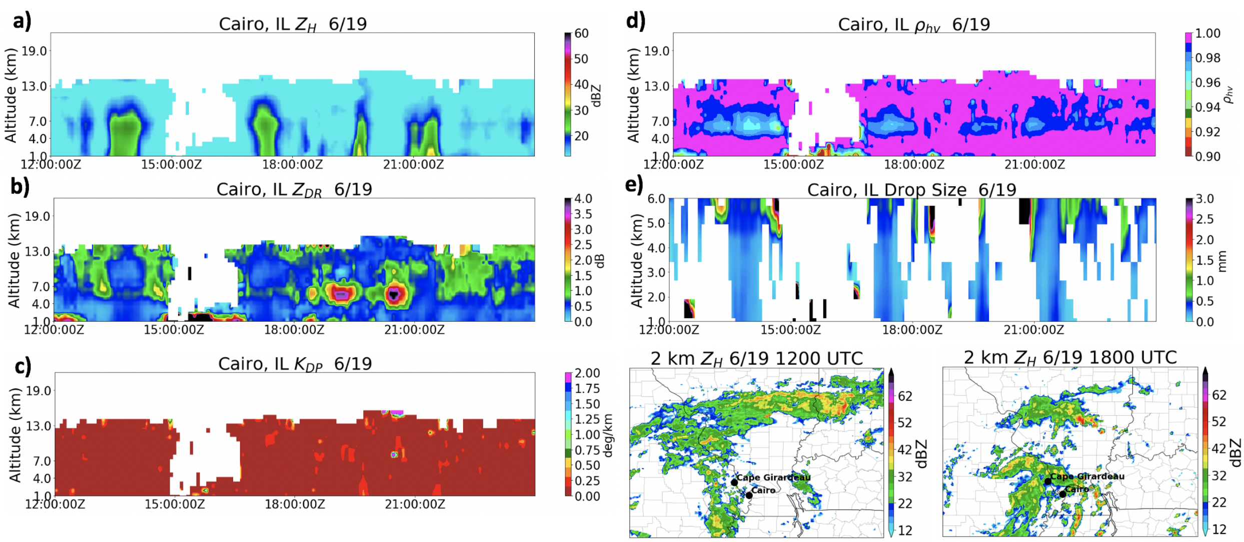

FIG. 8. Time-height curtains of Z_H (a), Z_{DR} (b), K_{DP} (c), ρ_{hv} (d), and drop size (e) during TCMI2 over Cairo, IL on from 1800 UTC 19 June-0000 UTC 20 June, and images of 2 km Z_H at 1200 UTC and 1800 UTC 19 June.

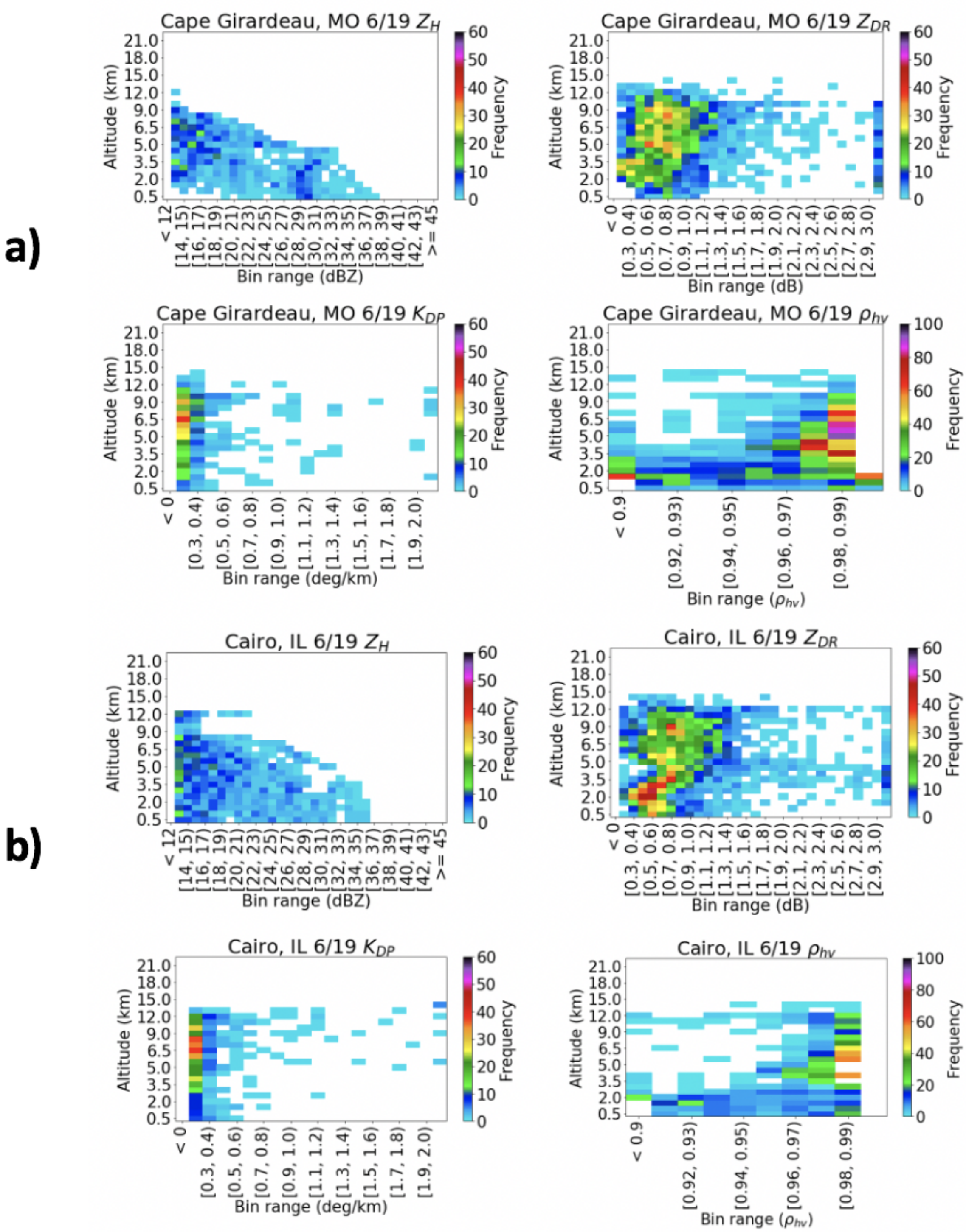

FIG. 9. Contoured Frequency By Altitude Diagrams (CFADs) of Z_H Z_{DR}, K_{DP}, and ρ_{hv} at Cape Girardeau, MO on 19 June (a), and Cairo, IL on 19 June (b) during TCMI 2.

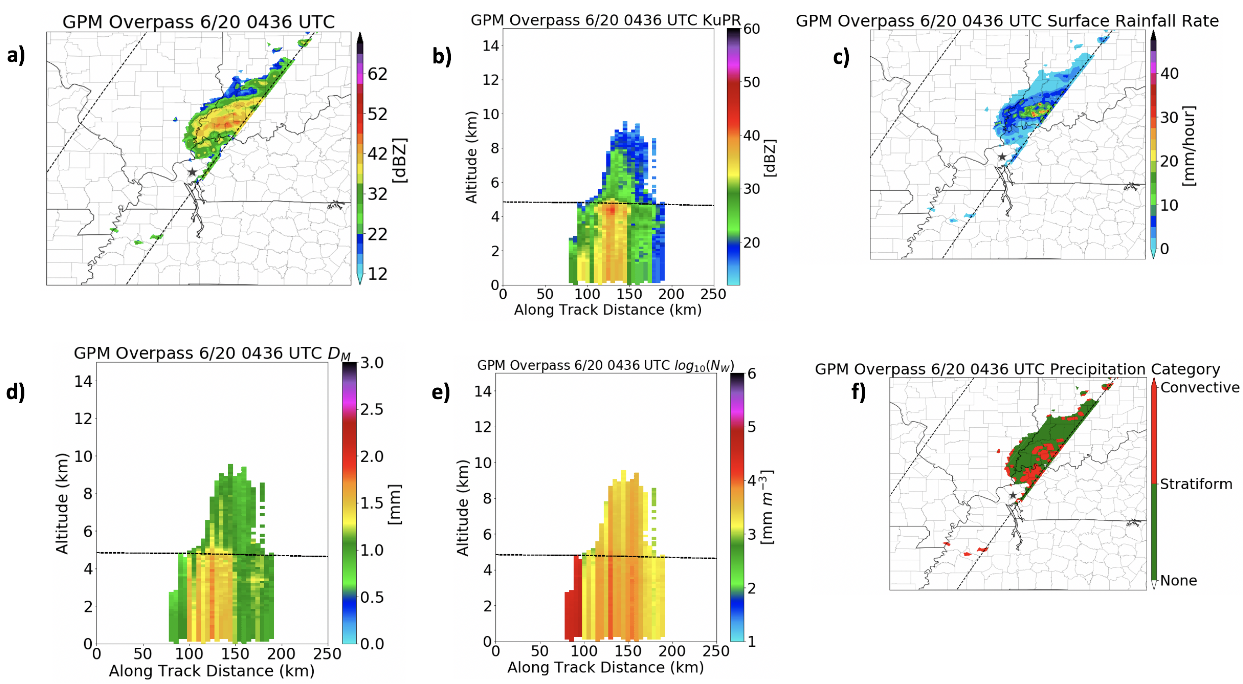

FIG. 10. GPM DPR near-surface reflectivity (a), GPM DPR along-track vertical profiles of $Z_M(Ku)$ (b), surface rainfall rate (c), D_M (d), $log_{10}(N_W)$ (e), and associated regions of stratiform and convective precipitation at 0436 UTC on 20 June, 2015 over Illinois (f). The dashed line represents the 0^oC isotherm.

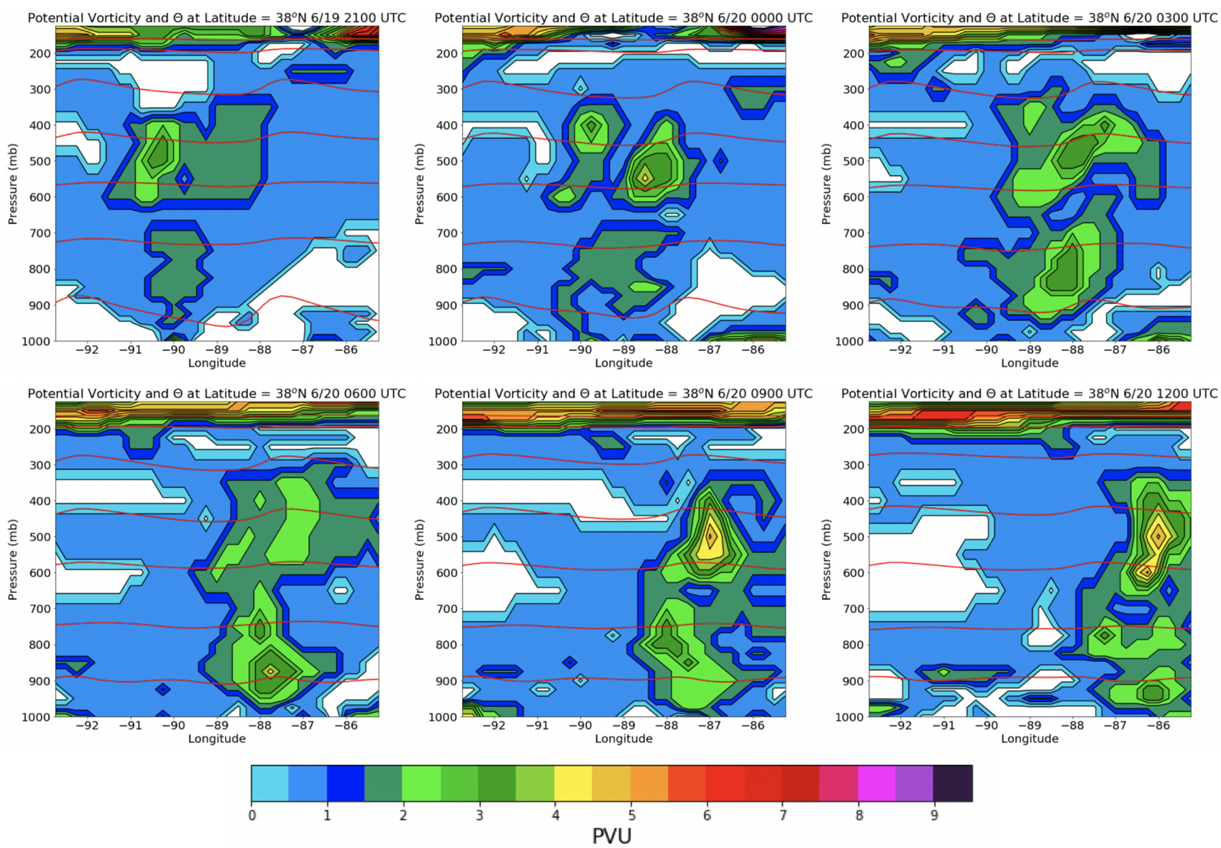

FIG. 11. Longitude-height cross-sections of potential vorticity (shaded) and potential temperature (contours) along 38^{o}N from 2100 UTC 19 June to 1200 UTC 20 June.

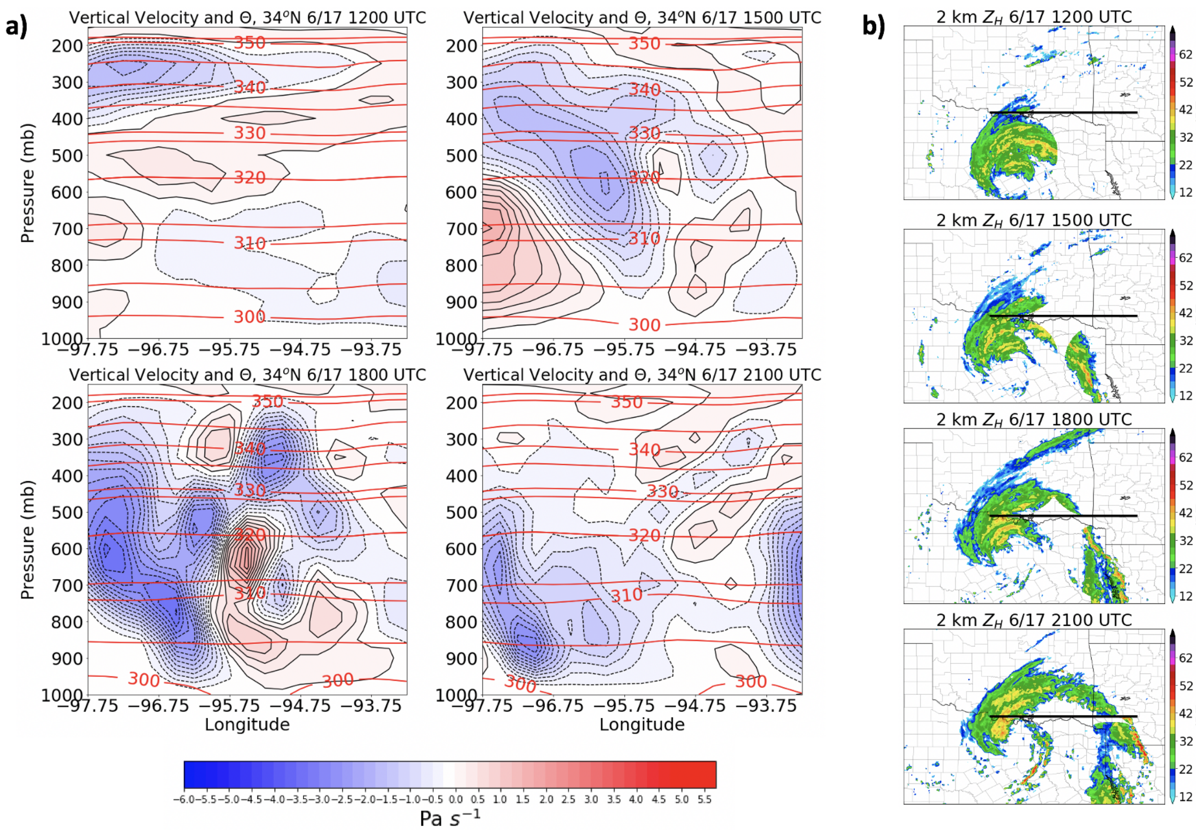

834 FIG. 12. Longitude-height cross-sections of vertical velocity (shaded) and potential temperature (contours)
835 along 34^oN from 1200-2100 UTC 17 June during TCMI1 (a), with snapshots of 2 km Z_H and cross-section
836 locations (b).

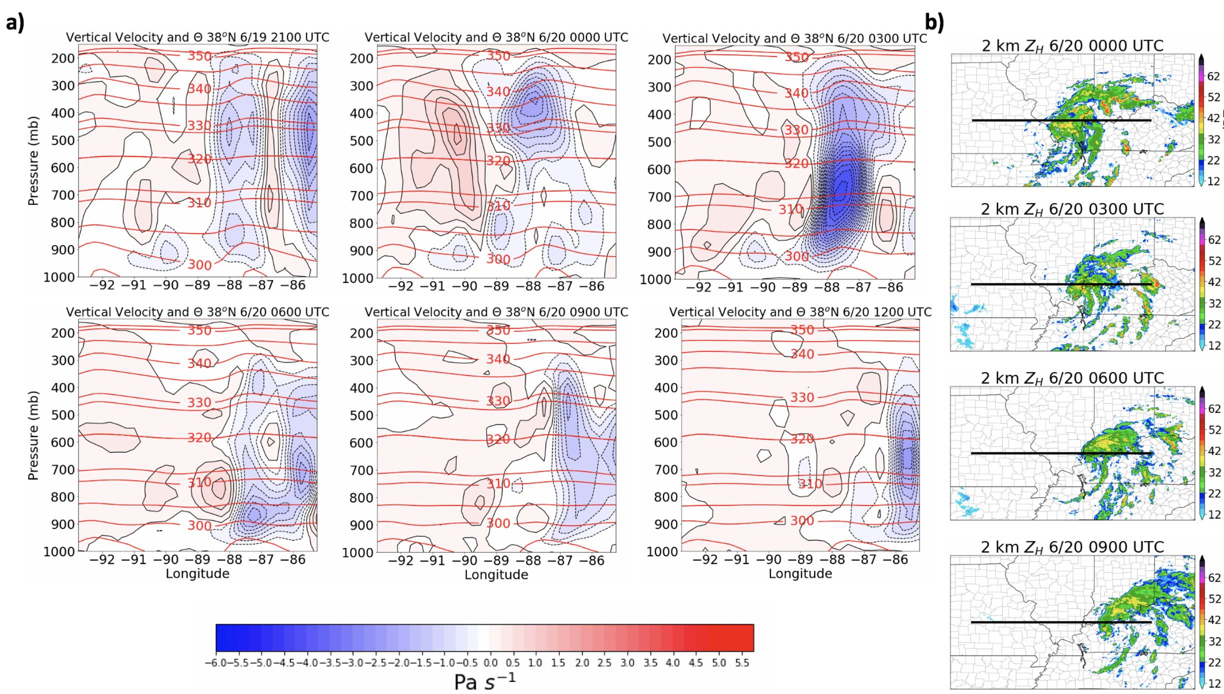

837 FIG. 13. Longitude-height cross-sections of vertical velocity (shaded) and potential temperature (contours)
838 along 38^{o}N from 2100 UTC 19 June to 1200 UTC 20 June during TCMI2 (a), with snapshots of 2 km Z_H and
839 cross-section locations (b).

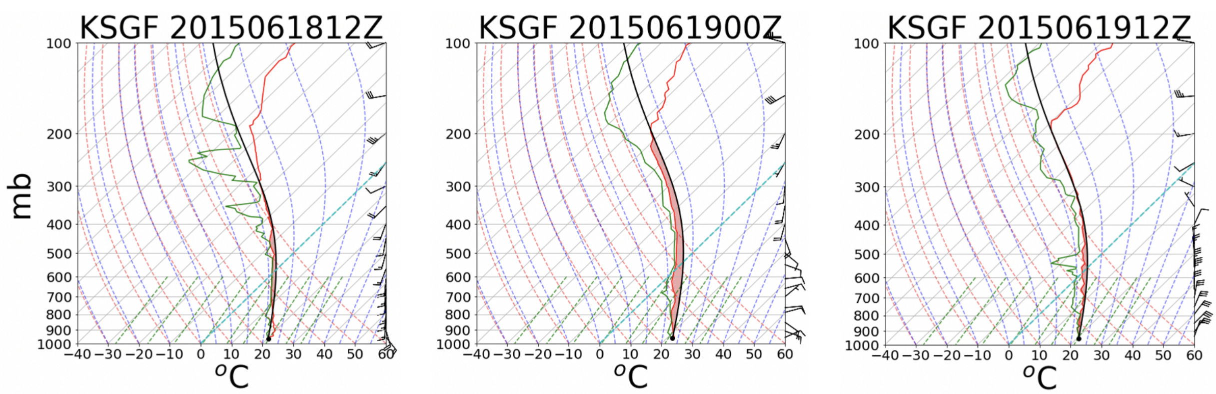

FIG. 14. Observed soundings from Springfield, MO from 1200 UTC on 18 June to 1200 UTC 19 June.